

The Mechanisms for the Onset and Explosive Eruption of Coronal Mass Ejections and Eruptive Flares

J. T. Karpen¹, S. K. Antiochos¹, and C. R. DeVore²

¹Code 674, NASA GSFC, Greenbelt, MD 20771

²Code 6042, NRL, Washington, DC 20375

Abstract

We have investigated the onset and acceleration of coronal mass ejections (CMEs) and eruptive flares. To isolate the eruption physics, our study uses the breakout model, which is insensitive to the energy buildup process leading to the eruption. We performed 2.5D simulations with adaptive mesh refinement that achieved the highest overall spatial resolution to date in a CME/eruptive flare simulation. The ultra-high resolution allows us to separate clearly the timing of the various phases of the eruption. Using new computational tools, we have determined the number and evolution of all X- and O-type nulls in the system, thereby tracking both the progress and the products of reconnection throughout the computational domain. Our results show definitively that CME onset is due to the start of *fast* reconnection at the breakout current sheet. Once this reconnection begins, eruption is inevitable; if this is the only reconnection in the system, however, the eruption will be slow. The explosive CME acceleration is triggered by *fast* reconnection at the flare current sheet. Our results indicate that the explosive eruption is caused by a *resistive* instability, not an ideal process. Moreover, both breakout and flare reconnections begin first as a form of weak tearing characterized by slowly evolving plasmoids, but eventually transition to a fast form with well-defined Alfvénic reconnection jets and rapid flux transfer. This transition to fast reconnection is required for both CME onset and explosive acceleration. We discuss the key implications of our results for CME/flare observations and for theories of magnetic reconnection.

1. Introduction

Understanding the mechanism for producing fast coronal mass ejections (CMEs) has challenged solar physicists for over three decades. These energetic explosions always originate in filament channels, where the necessary free energy is stored, and usually are accompanied by eruptive multi-ribbon flares, prominence eruptions, interplanetary shocks, and solar energetic particles. The unique magnetic structure of a filament channel (Martin 1998; Gaizauskas 2001) – a region of strong magnetic nonpotentiality narrowly collimated around a polarity inversion line (PIL) – plays the critical role here, but the exact topology remains controversial. There are two principal classes of models for the magnetic configuration of filament-channel fields before eruption: twisted flux ropes and sheared arcades (see review by Mackay et al. 2010). For these initial configurations, the eruption onset has been attributed to either a loss of equilibrium/ideal instability (e.g., Forbes & Isenberg 1991; Török & Kliem 2005; Rachmeler et al. 2009) or magnetic reconnection (e.g., Sturrock 1989; Amari et al. 2000; Moore et al. 2001; Roussev 2007; Titov et al. 2008). In general, the ideal models require the presence of a twisted flux rope prior to eruption, whereas the reconnection models can operate with either a twisted flux rope or a sheared arcade (Forbes et al. 2006).

Our “breakout” model provides an intuitive and straightforward mechanism for fast CME initiation. Breakout invokes reconnection to disrupt the force balance that maintains the highly sheared filament channel field in the corona (Antiochos et al. 1994; Antiochos 1998; Antiochos et al. 1999; MacNeice et al. 2004; Lynch et al. 2004, 2005; DeVore & Antiochos 2005, 2008; DeVore et al. 2005; Phillips et al. 2005; Roussev et al. 2007; van der Holst et al. 2007, 2009; Lynch et al. 2008, 2009; Zuccarello et al. 2008, 2009a; Jacobs et al. 2009; Soenen et al. 2009). Numerous well-observed solar eruptions agree qualitatively with the topology and expected dynamical evolution of the breakout model (Aulanier et al. 2000; Sterling & Moore 2001a,b, 2004a,b; Manoharan & Kundu 2003; Gary & Moore 2004; Deng et al. 2005; Williams et al. 2005; Alexander et al. 2006; Mandrini et al. 2006; Sui et al. 2006; Joshi et al. 2007; Lin et al. 2010; Aurass et al. 2011). On the other hand, some observed CMEs have been interpreted to be inconsistent

with the breakout scenario (e.g., Ugarte-Urra et al. 2007; Zuccarello et al. 2009b; Cheng et al. 2010; Seaton et al. 2011).

The breakout model, illustrated by Figure 1, requires only three basic ingredients (Antiochos et al. 1999):

1. The magnetic topology has two or more flux systems (at least two PILs on the photosphere, as is always observed), so that reconnection can transfer flux from one system to another. The corona never consists of a single flux system; magnetic extrapolations generally find several topologically distinct systems (e.g., Roussev et al. 2007; Cook et al. 2009). The field of Figure 1a is the simplest multi-flux topology, consisting of just two flux systems with the well-studied coronal null point, fan separatrix surface, and pair of spine lines (e.g., Antiochos 1990; Lau & Finn 1990; Priest & Titov 1996). This topology is observed to be ubiquitous in the corona, dating back as far as Skylab (e.g., Tousey et al. 1973; Sheeley et al. 1975).

2. A filament channel forms (magnetic free energy is added) slowly. In our simulations we form a filament channel by applying a slow photospheric shear flow localized about the PIL of the strong-field active region. Such shear flows are sometimes, but not always, observed (e.g., Hindman et al. 2006; Rondi et al. 2007; Kazachenko et al. 2009); shear flows at the PIL also accompany flux emergence from the convection zone into the corona, as shown by recent 3D MHD simulations (Fang et al. 2012). The key point is that this simplest possible driver introduces no new physics to the system. Its form (shear profile, temporal behavior, etc.) is irrelevant to the eruption (e.g., Phillips et al. 2005): all that matters is the total free energy. Therefore, we can isolate and study the eruption mechanism without first having to understand the unknown filament-channel formation process or impose *ad hoc* boundary conditions.

3. The resistivity is scale dependent. Diffusion always has strong scale dependence, but in our simulations, the numerical resistivity coefficient itself is scale dependent. Our MHD code, *ARMS* (§2), applies a second-order diffusion term wherever the solution develops structure down to the grid scale (DeVore 1991). This diffusion term is independent of plasma parameters and can become as large as needed locally to maintain a smooth solution. For the mostly collisionless corona, the breaking of field lines is

expected to occur at spatial scales where kinetic processes dominate (e.g., the ion skin depth or gyroradius), so the true coronal resistivity is also scale dependent. Unlike our numerical resistivity, however, the magnitude of coronal resistivity does depend on plasma and magnetic field parameters, which may affect the eruption process. Incorporating a rigorous kinetic resistivity into a global CME model is not feasible at present; consequently, in this study we simply used the numerical resistivity.

Given the three ingredients above, eruption is inevitable (see §3.2). The addition of the low-lying shear pushes the overlying flux systems (red and blue in Fig. 1) together, causing a current sheet (denoted the breakout current sheet) to appear at the null and along the separatrix between them (Fig. 1b). Once this breakout sheet thins down sufficiently, the numerical resistivity “switches on” and breakout reconnection begins to remove overlying flux by transferring it to the sides (converting blue and red flux to green; Fig. 1b). The resulting decrease in the downward tension causes the sheared field to expand faster, thereby creating a feedback loop that accelerates eruption. When the flux has expanded outward sufficiently, a vertical current sheet (denoted the flare current sheet) forms low in the corona (Fig. 1c). This feature is common to almost all CME models, not only breakout. The reconnection at the flare sheet relaxes the magnetic field back toward its minimum-energy potential state.

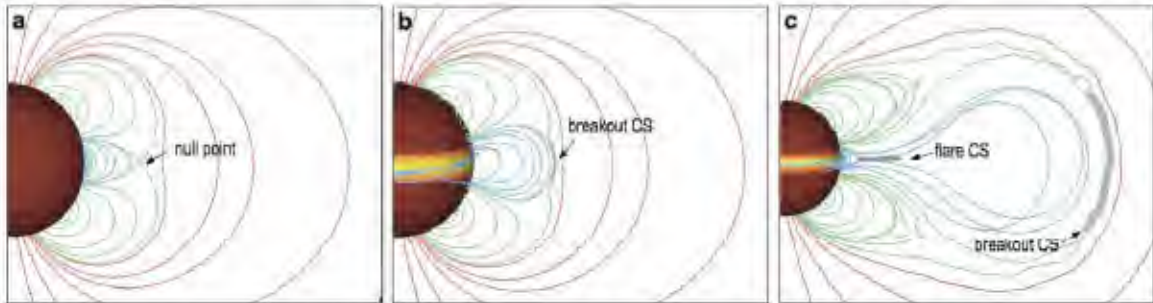


Figure 1. Selected magnetic field lines at 3 times during the main simulation, illustrating the key structures of the breakout model including current sheets (CS). Red lines indicate overlying field; green indicates side lobe field lines; and blue indicates core field lines. All field lines are drawn from the same set of footpoints. Gray lines show the general locations of the flare and breakout current sheets. The spherical surface is at $1 R_{\odot}$, with shading from red to yellow indicating increasing azimuthal field strength. a) $t=0$ s. b) $t=72,500$ s (before onset of flare reconnection). c) $t=102,500$ s (during the impulsive phase of flare reconnection).

Reconnection thus plays two roles in the breakout scenario: in addition to the removal of restraining flux through breakout reconnection, the core flux comprising the CME becomes partially detached from the Sun through flare reconnection. The flare

reconnection transfers core flux into both the CME and a compact, growing arcade rooted around the PIL. This post-eruption arcade contains the X-ray loops, H α ribbons, and other classic signatures of an eruptive flare. Our earlier studies indicated that the flare is a critical component of the eruption: breakout reconnection alone generally did not produce a fast ejection. Hence, understanding the development of both current sheets, and the conditions triggering and stopping reconnection in these sheets, is the key to understanding energy release in CMEs and eruptive flares.

The goals of this work are to determine the conditions leading to breakout and flare reconnection, and to quantify and understand the relationship between breakout and flare reconnection, in particular their roles in producing a fast eruption. Prior studies demonstrated the basic viability of the breakout scenario in both 2D and 3D geometries using static, non-uniform grids (e.g., MacNeice et al. 2004; Lynch et al. 2004, 2008; van der Holst et al. 2009). These computational investigations agreed on the general link between flaring and fast CME acceleration, but were not well equipped to pinpoint the exact timing and locations of critical events such as flare reconnection onset. In addition, because current sheets are discontinuities on the MHD scale, studying their detailed development computationally requires the highest resolution possible in multiple regions that evolve fully dynamically. Moreover, although reconnection in idealized current sheets has been studied extensively and with ever-increasing dynamic range (e.g., Bhattacharjee et al. 2009; Daughton et al. 2009), those results are not directly applicable to the CME problem because there is no pre-existing static current sheet in the solar case; coronal current-sheet formation cannot be separated from the global evolution of the filament-channel field.

Therefore, in this paper we take the next critical step in our study of breakout CMEs: high-resolution simulations employing full adaptive mesh refinement (AMR). Here we present and interpret one simulation with up to six levels of refinement, deferring a discussion of the effects of grid refinement level on the CME and flare properties to a later paper. By examining the numerical results during key activity periods with high cadence, and employing new tools to identify and track multiple nulls, we have revealed the critical interdependence between CME acceleration and flare reconnection. Our results bring into question prior assumptions about the role of reconnection and the nature

of the eruption process itself. In particular, we find that a resistive instability is responsible for triggering the explosive eruption.

2. Numerical Model

The multidimensional numerical simulations were performed with our Adaptively Refined Magnetohydrodynamics Solver (*ARMS*). *ARMS* employs a finite-volume representation of the plasma and magnetic field and the high-fidelity, Flux-Corrected Transport techniques (DeVore 1991) that have long been used to ensure the accuracy and positivity of solutions to the nonlinear MHD equations. *ARMS* also initializes the solution, applies the boundary conditions as the variables are advanced in time, and periodically tests the adequacy of the grid resolution. NASA's *PARAMESH* toolkit for parallel adaptive mesh refinement (MacNeice et al. 2000) provides a robust, powerful capability to adapt the grid dynamically as the solution evolves in time. The mesh is constructed of a large number of grid blocks with a fixed number of cells per block, but with the physical size of each block varying with refinement level. These blocks can be subdivided or recombined as needed to maintain a desired resolution of developing small-scale structures, without creating or unnecessarily retaining superfluously fine resolution of the large-scale structures.

For the present work, *ARMS* solved the following equations of ideal MHD in spherical coordinates:

$$\begin{aligned}\frac{\partial \rho}{\partial t} + \nabla \cdot \rho \mathbf{v} &= 0 \\ \frac{\partial \rho \mathbf{v}}{\partial t} + \nabla \cdot \rho \mathbf{v} \mathbf{v} &= -\nabla P + \frac{1}{4\pi} (\nabla \times \mathbf{B}) \times \mathbf{B} + \rho \mathbf{g} \\ \frac{\partial T}{\partial t} + \nabla \cdot T \mathbf{v} &= (2 - \gamma) T \nabla \cdot \mathbf{v} \\ \frac{\partial \mathbf{B}}{\partial t} - \nabla \times (\mathbf{v} \times \mathbf{B}) &= 0\end{aligned}$$

All of the symbols have their standard meanings: ρ is the mass density, \mathbf{v} the velocity, P the thermal pressure, T the temperature, \mathbf{B} the magnetic induction, and t the time. We assumed a fully ionized hydrogen plasma whose ratio of specific heats $\gamma = 5/3$ and used

the solar gravitational acceleration $\mathbf{g} = -GM_s\mathbf{r}/r^3$, where M_s is the solar mass, G the universal gravitational constant, and \mathbf{r} the position vector. The temperature equation describes simple adiabatic heating or cooling of the plasma as it compresses or expands. There are necessary, stabilizing numerical diffusion terms implicit in solving all of these equations; those in the induction equation permit magnetic reconnection to occur at current sheets that thin down to the finite scale of the simulation grid.

We assumed a spherically symmetric initial atmosphere in hydrostatic equilibrium with the prescribed temperature profile

$$T(r) = T_s \frac{R_s}{r},$$

where $T_s = 2 \times 10^6$ K. The equilibrium is solved exactly on the finest grid accessible to the simulation and injected conservatively onto coarser grids to preserve pressure balance across any latitudinal jumps in the grid refinement level. We assumed a base pressure $P_s = 5.5 \times 10^{-2}$ dyn cm⁻². The initial potential magnetic field is a superposition of the dipole and octupole spherical harmonics, with the radial component at the solar surface given by

$$B_r(R_s, \theta) = B_0 (2 \cos^3 \theta - \cos \theta),$$

where $B_0 = 10$ G is the maximum initial field strength at the solar poles. An imposed longitudinal shearing flow obeys the simple sinusoidal profile

$$v_\varphi(R_s, \psi) = v_0 \begin{cases} \sin(\pi\psi/\psi_0); & |\psi| \leq \psi_0 \\ 0; & \text{otherwise} \end{cases}$$

where $\psi = \pi/2 - \theta$ is the solar latitude, $\psi_0 = \pi/8$, and $v_0 = 20$ km s⁻¹. These subsonic, sub-Alfvénic motions gradually formed a filament channel concentrated about the equator. We smoothly ramped the flows up and down using a sinusoidal time profile of duration 100,000 s, which yields a peak displacement of $\pi/2$ radians in each hemisphere at latitudes $\pm \psi_0/2$.

The 2.5D simulations discussed in this paper assume spherical axisymmetry. The inner radial boundary is the solar surface ($1 R_s$) while the outer boundary is at $125 R_s$, and the grid is exponentially stretched in the radial direction. The initial grid blocks are uniformly spaced in colatitude θ , which runs from 0 at the north pole to π at the south. For our

simulation with up to six levels of refinement (§3), the radial cell length ranges from about 2 Mm to $3 R_{\odot}$, and the latitudinal cells vary in extent between $\pi/1024$ and $\pi/128$. A sixteen-cell-high (two grid blocks) zone of the smallest cells was maintained just above the solar surface, to ensure that the flows and fields there are well resolved throughout the simulation. Elsewhere, the grid was refined as needed to provide the minimum required resolution at current sheets, shocks, and other discontinuities. The criteria for dynamic regridding are discussed in the Appendix.

The robustness of the regridding can be seen in Figure 2, which plots the grid superposed over contours of current magnitude. Note that the grid is maximally refined where the currents are largest and, even more importantly, the grid is coarse where they are small. Implementing effective procedures for derefining the grid is often more challenging than simply refining.

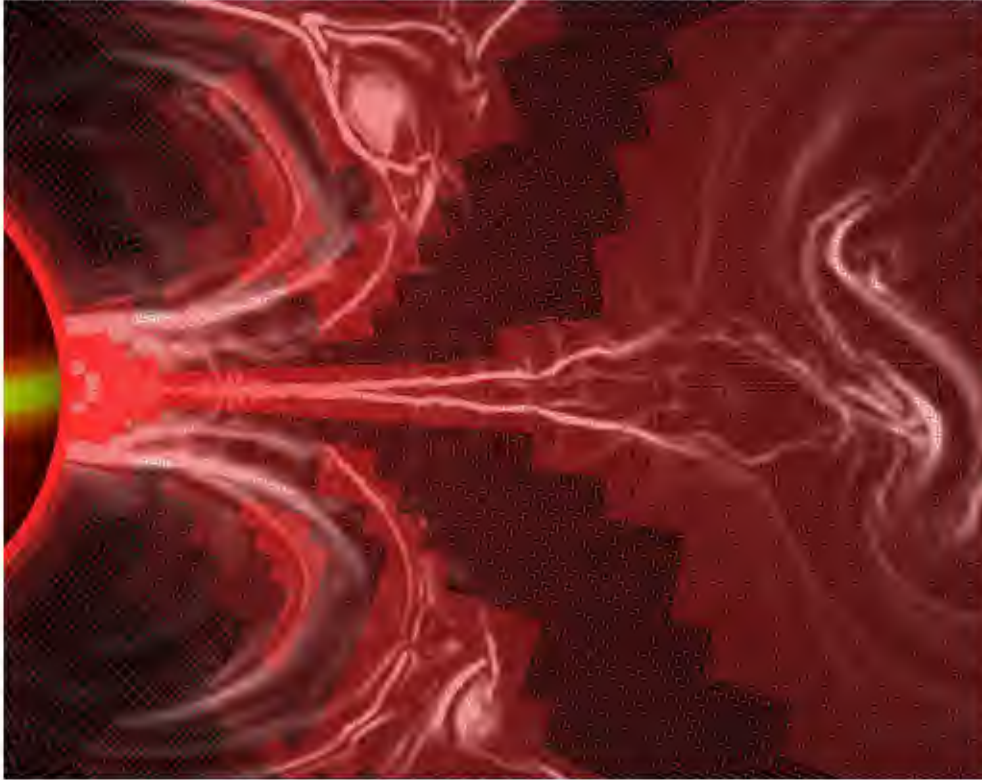


Figure 2. Close-up view of the current structures below the CME at $t=102,500$ s. Grayscale image of coronal current magnitude (see Fig. 3 for details) with grid (red squares) superposed, showing the fidelity of the adaptive mesh to capture important current structures. Post-eruption loops are at left, erupting flux-rope CME is at right. At far left, the colors on the solar surface indicate the magnitude of the shear component of the magnetic field, B_s , around the polarity inversion line (max. = yellow, min. = red).

Closed boundary conditions (no inflow, outflow, or diffusion) were imposed at the inner radial boundary and at both poles, while the outer radial boundary is open to flow and diffusion. Zero-gradient conditions were applied to ρ and T at the poles, while multiplicative factors set by the initial hydrostatic equilibrium atmosphere were used for those scalars at both radial boundaries. Reflecting conditions were imposed on v_θ and v_ϕ at the poles, and free-slip conditions were applied to v_r . At the inner radial boundary, v_r and v_θ are reflecting, while v_ϕ is the shearing flow prescribed above; thus, the magnetic field is line-tied there. The velocity vector \mathbf{v} floats freely at the outer radial boundary, allowing both slippage and outflow. Zero-gradient conditions were applied to the vector magnetic field \mathbf{B} at the inner and outer radial boundaries and to the radial component B_r at the poles, where reflecting conditions were imposed on B_θ and B_ϕ .

3. Results

We used *ARMS* to perform a breakout CME simulation with a maximum of six levels of grid refinement. Figure 3 and the accompanying movie show the global evolution of the system, which generally agrees with earlier 2.5D breakout calculations. For this high-resolution simulation, however, the evolution divides clearly into three distinct phases defined by the onset of fast reconnection at the breakout and flare current sheets. The first phase is almost ideal, consisting of a quasi-static expansion driven by the shear buildup in the filament channel (Fig. 3a). The expansion leads to current sheet formation at the null point and separatrices, and very weak reconnection there (Fig. 3b). This quasi-ideal evolution ends with the onset of fast reconnection at the breakout current sheet, which produces a second phase of slow eruption (Fig. 3c). During this second phase, reconnection begins at the flare current sheet, forming slowly evolving islands. This phase ends with the onset of fast reconnection at the flare sheet, producing the final explosive eruption phase (Fig. 3d).

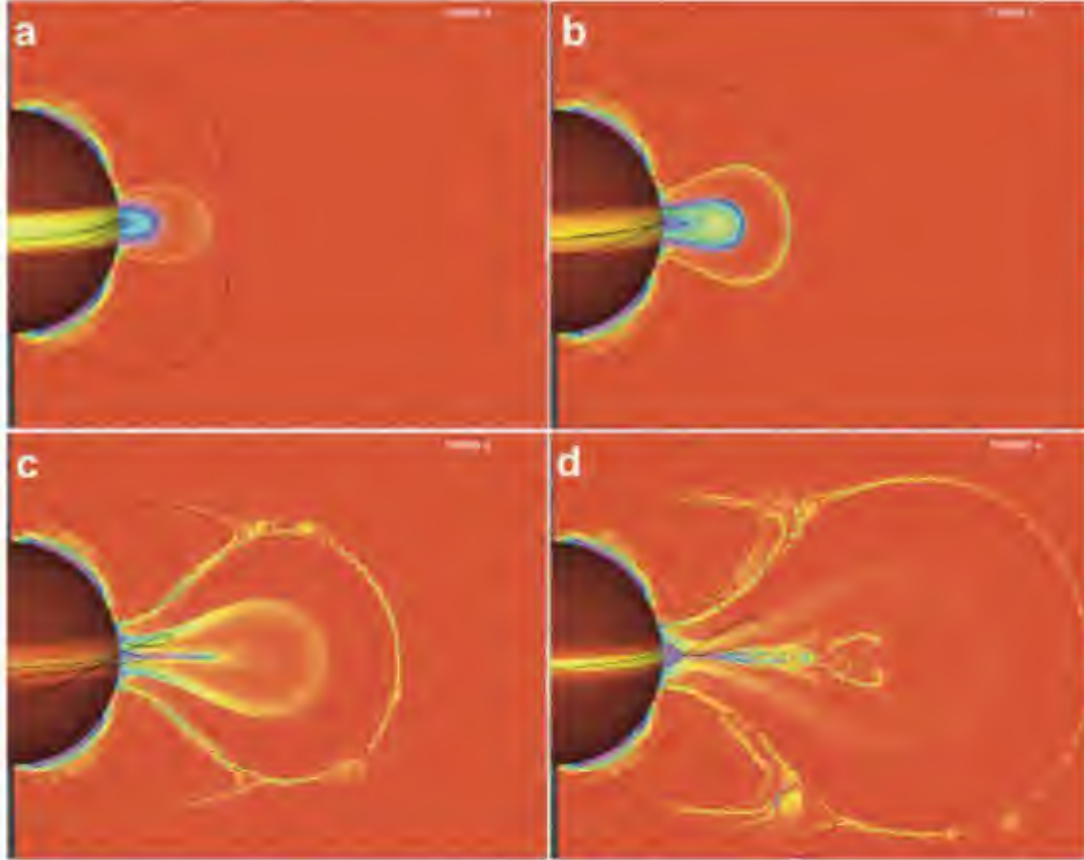


Figure 3. Photospheric B_ϕ (red-yellow contours on the $r=R_s$ surface), normalized current density magnitude $R_s|J|/c$ in the r - t plane (red to magenta), grid blocks (white lines), and magnetic field lines (black) in the simulation at selected times. a) 50,000 s. b) 75,000 s. c) 90,000 s. d) 100,000 s. The full temporal evolution is shown in the movie available in the electronic edition (movie1.mpg). The minimum B_ϕ (dark red) is zero; the maximum value (yellow) is saturated at 2 G. The minimum value of $R_s|J|/c$ (red) is zero; the maximum value (magenta) is saturated at 0.2 G.

The important evolution of the magnetic shear injected into the system is evident in Figure 3. The contours on the photospheric surface correspond to magnitude of the shear component of the field, B_ϕ . Comparison of panels (a) and (d) shows that the ejection reduces the width of the strong-shear zone. In fact, this indicates the basic reason for the eruption in our simulation and for all real CMEs/eruptive flares. The magnetic shear of a filament channel is a form of helicity; therefore, reconnection can only redistribute the shear, not eliminate it. In order to decrease substantially the free energy in filament channels, the Sun must eject the sheared flux out into the far heliosphere. The evolution shown in Figure 3 is simply the process of expelling the shear, and then relaxing the field back to a near-potential state. As in real solar events, where the eruption rarely extends

down to the photospheric PIL, some very low-lying sheared flux remains behind as seen in panel (d).

To understand the various phases of the eruption in detail, we plot in Figure 4 the evolution of the volume-integrated magnetic and kinetic energy in the system, along with key times marked by vertical lines. Figure 4 encapsulates the main results of this paper. We clearly see the three phases of the eruption in the evolution of the kinetic energy: first, the quasi-static expansion leading to the onset of fast breakout reconnection (cyan blue vertical dashed line); second, the phase of slow eruption leading to the onset of fast flare reconnection (green line); and finally, the explosive CME “takeoff.”

A critical conclusion drawn from our results is that *CME onset corresponds to the start of fast breakout reconnection*. Once this reconnection begins, eruption is inevitable. On the other hand, Figure 4 clearly shows that *the trigger for the explosive CME take-off (fast acceleration) is the onset of fast flare reconnection*, not the breakout reconnection.

Figure 4 also shows the evolution of the magnetic energy during the three phases of the eruption. During the quasi-static first phase, the injection of shear causes the magnetic energy to increase monotonically, reaching its maximum value during the second, breakout-reconnection phase ($\sim 73,000$ s). The maximum magnetic free energy is $\sim 11\%$ of the energy of the *total* initial potential field (including the side flux systems). Note that the shear flows still are injecting energy into the corona at 73,000 s but they are ramping down (until $t = 100,000$ s), whereas the magnetic energy losses due to expansion and reconnection continue to increase, so that they surpass the energy input rate at this time. The magnetic energy decreases slowly, with only a small amount of magnetic energy expended, until the onset of fast flare reconnection. Then a dramatic change in the global energy balance ensues, with rapid conversion of magnetic energy into plasma energy. Approximately 73% of the total magnetic free energy is converted to other forms of energy, including kinetic energy (Fig. 4).

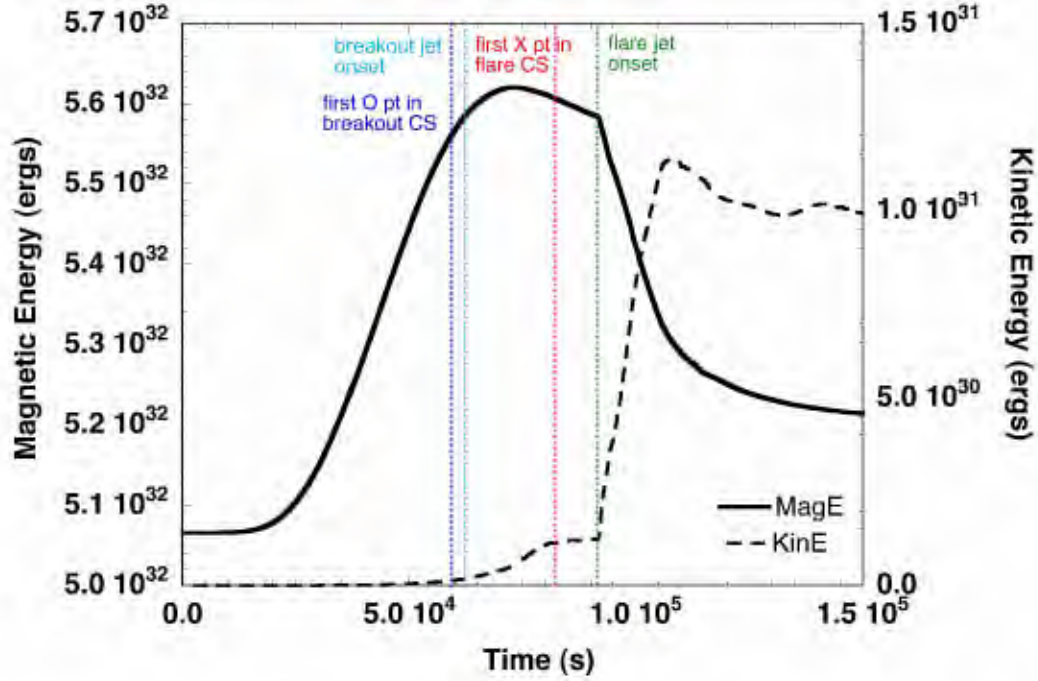


Figure 4. Volume-integrated kinetic and magnetic energies vs. time. Vertical lines denote important milestones in the CME/flare evolution, which are discussed in detail in the text.

Figure 4 also reveals that null points appear in the current sheet well before the onset of fast reconnection with observable plasma jets, in both breakout and flare reconnections (especially in the flare). Therefore the reconnection in our system has two distinct forms: a preliminary tearing-like form characterized by the formation of small, nearly-stationary plasmoids (magnetic islands), followed by a strongly dynamic form with Alfvénic jets and multiple islands ejected from the current sheet. This latter form resembles geometrically the classical Sweet-Parker model in that it involves a long current sheet, but the reconnection is fast, $\sim 10\% V_A$, and dominated by magnetic islands. We discuss in more detail below the evolution of the system during the three phases.

3.1 The Quasi-Ideal Buildup Phase

The shear flows that inject free energy into our system were applied for 100,00 s with a sinusoidal profile (§2). These flows cause the inner flux system to expand outward quasi-statically, increasing the magnetic free energy (Fig. 4) and deforming the null point into a current sheet exactly as in the classic Syrovatskii model (Syrovatskii 1971, 1978a,b, 1981). As shown in Figure 5, the average speed immediately behind the

breakout sheet during this rise phase from 50,000 to 60,000 s is $\sim 13 \text{ km s}^{-1}$, which is over an order of magnitude smaller than the Alfvén speed there.

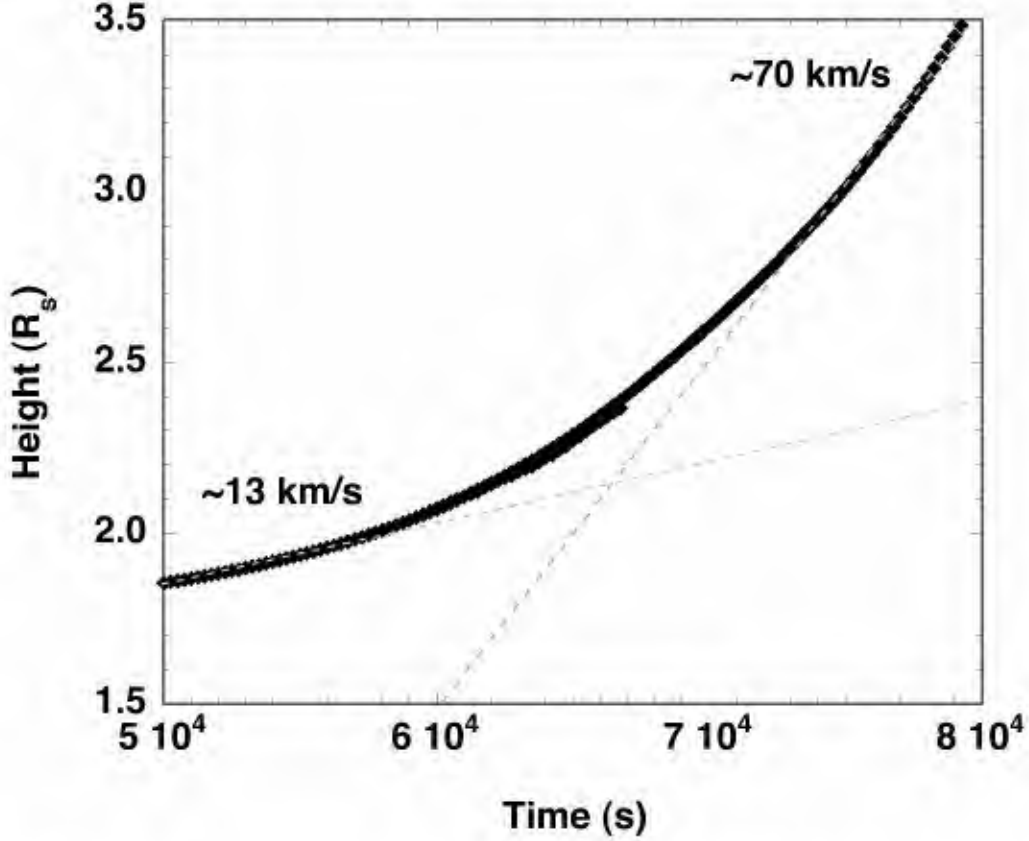


Figure 5. Height of the cavity front vs. time during the preflare phase. The front is defined as the location of the X-type null nearest the equator in the breakout current sheet. Dotted lines show linear fits to the height at the beginning and end of the phase, to indicate the speed increase, although the actual acceleration clearly is smooth.

Figure 6 shows the evolution of the width of the breakout current sheet. For the parameters of this particular simulation, the current sheet thins down to the grid scale at approximately 57,500 s, followed by continuous slow erosion of the overlying/underlying flux (red and blue flux in Fig. 1) through reconnection at the stressed null point. After 57,500 s we clearly see the continuous transfer of flux between systems. Although the evolution is not purely ideal, this flux transfer is driven slowly by the outward expansion resulting from the footpoint shear, and does not correspond to instability. In fact, the magnetic energy continues to increase during this time (Fig. 4).

The important point is that, once the current sheet thins down to the grid scale (Fig. 6), it stays at that scale even during the most vigorous breakout reconnection. The feedback

between expansion and reconnection (Antiochos et al. 1999) explains this balancing act: reconnection weakens the sheet, but reconnection also induces faster outward expansion, which strengthens the sheet.

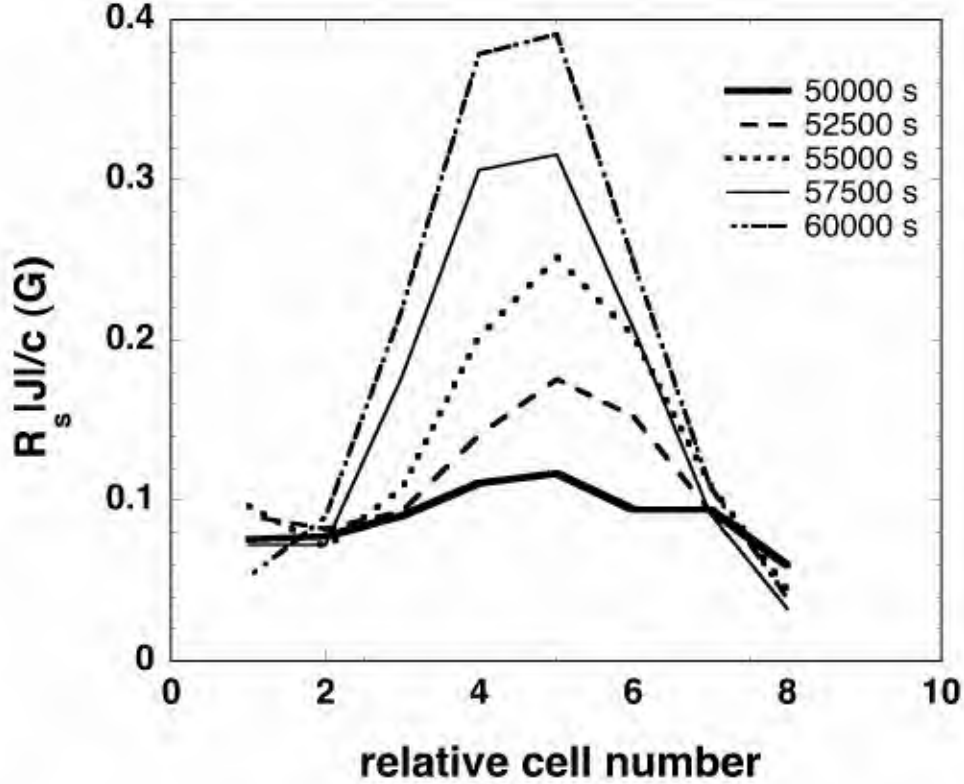


Figure 6. Radial cuts through the normalized current density magnitude $R_s |J|/c$ in the vicinity of the central X point in the breakout current structure, at successive times during the preflare phase. With the averaging involved in calculating and visualizing $|J|$, a minimum-width current sheet will appear to have a full width at half maximum of two cells.

3.2 The Breakout-Driven Eruption Phase

The quasi-ideal phase ends and the breakout phase begins with an abrupt change in behavior that we denote “breakout onset”: reconnection jets (Alfvénic outflows) appear at the ends of the breakout sheet, and the integrated kinetic energy of the system begins to rise (Fig. 4). The sheet itself also exhibits a substantial increase in outward motion, accelerating to $\sim 70 \text{ km s}^{-1}$ by 80,000 s (Fig. 5). This faster expansion forces the breakout current sheet to continue to strengthen (Fig. 6). The feedback between expansion and breakout reconnection alone would produce a complete but slow ejection: it would leave

behind a vertical current sheet extending downward to very low heights in the corona, thus containing a large fraction of the initial free energy.

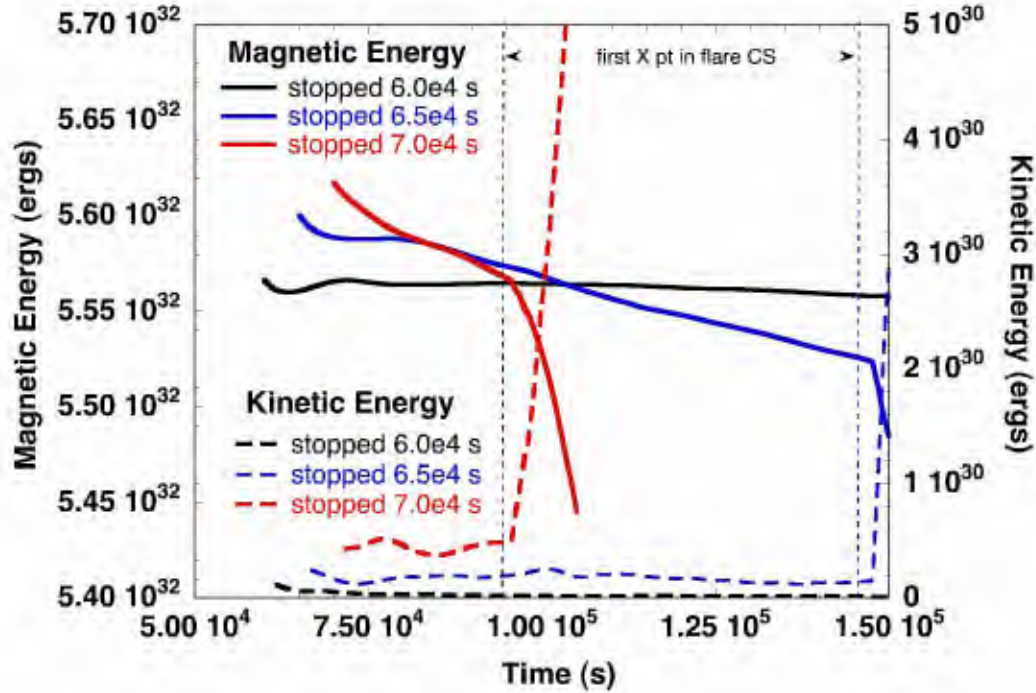


Figure 7. Integrated kinetic energies (dashed lines) and magnetic energies (solid lines) for test calculations described in the text. In these runs, the main calculation was restarted with photospheric footpoint motions turned off at the indicated times, and the system was allowed to relax thereafter.

The fundamental factor determining whether or not our system erupts is the amount of available magnetic free energy (e.g., Phillips et al. 2005). Because our simple mechanism for supplying free energy (i.e., footpoint displacement) continued from $t=0$ well into the flare onset phase, however, we could not determine the threshold energy for eruption with the main calculation alone. Consequently, we performed three test calculations in which the main calculation was stopped at selected times, restarted, and allowed to evolve without further shearing. These times were chosen to be close to the breakout onset time: 60,000 s, 65,000 s, and 70,000 s. As shown in Figure 7, only the simulation in which shearing was stopped at 60,000 s failed to erupt, demonstrating that sufficient free energy to power the eruption was accumulated by some time between 60,000 and 65,000 s. The case where shearing was stopped at 65,000 s remained in the pre-flare state until $\sim 147,500$ s, while CME/flare onset in the 70,000-s case began only $\sim 3,000$ s later than the main calculation (where shearing was continued until 100,000 s). It is important to note that the non-erupting case showed no evidence of fast reconnection jets associated

with breakout reconnection, whereas the erupting cases exhibited Alfvénic flows at the ends of the breakout sheet and gradual loss of integrated magnetic energy between the start of fast breakout reconnection and flare reconnection/CME onset. These results confirm our conjecture that the presence of fast breakout reconnection signals CME onset – the point when eruption becomes inevitable – and are consistent with our earlier simulations (e.g., Antiochos et al. 1999).

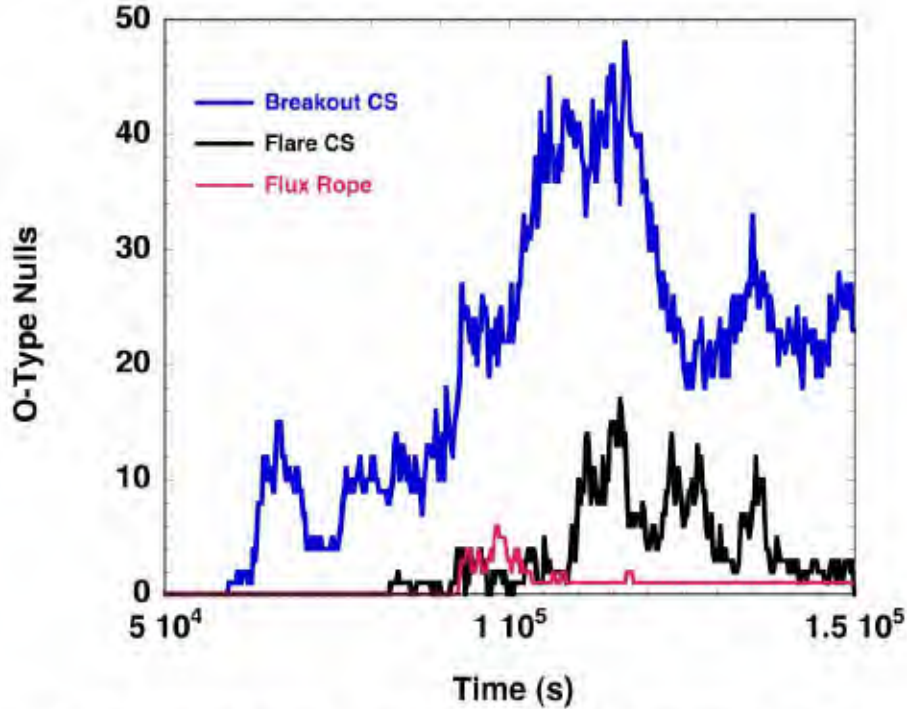


Figure 8. Number of O-type nulls as a function of time in the breakout current sheet (blue line), flare current sheet (black line), and flux rope/CME (red line).

The evolution of the nulls in the breakout and flare current sheets provides a critical diagnostic of the reconnection dynamics. The first O-type nulls¹ form at the breakout current sheet at 59,250 s (Fig. 8), shortly before the onset of fast reconnection jets (Fig. 4). Because the breakout sheet begins as an X-type null, the appearance of the first O-type null is the definitive indicator of reconnection. As shown in Figure 8, the instantaneous number of O points in the breakout sheet reaches a local maximum of 15 around 66,500 s, drops to a plateau value of 4 from ~70,000–75,000 s, then rises on

¹ For convenience we will use the terms O-type null, O point, and magnetic island (similarly, X-type null and X point) interchangeably in this paper, although this is strictly correct only in 2D systems.

average through the remainder of the breakout-driven phase. A pair of islands near the equator dominates the breakout sheet structure during the minimum plateau, eventually merging by $\sim 85,000$ s (see movie1.mpg accompanying Fig. 3). Few vestiges of the initial north/south symmetry remain thereafter, since the merged island drifts below the equator and the erupting flux system bulges at southern latitudes. This symmetry breaking allows the formation of new islands to resume at an accelerated pace.

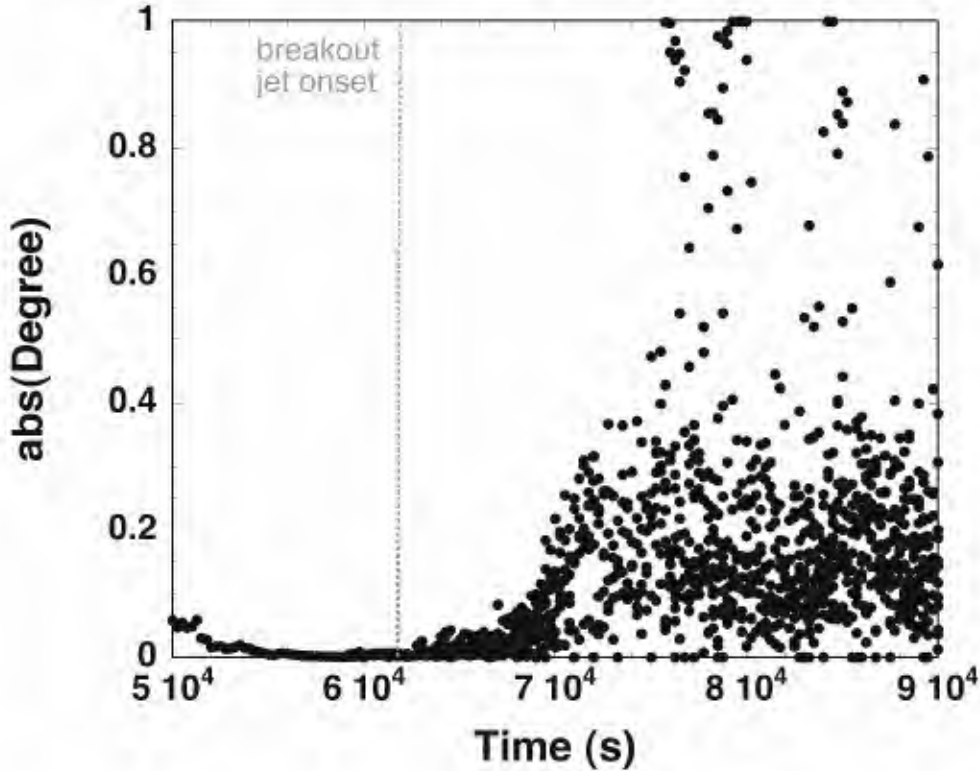


Figure 9. Absolute value of degree D (see Appendix) of X-type nulls in the breakout current sheet during the quasi-ideal and breakout-driven phases. Each black dot at a specific time represents an individual null.

The distinguishing property of the null points is their degree D , defined in the Appendix and plotted in Figure 9. The degree of a null indicates its shape: for example, a classic potential X-type null with an opening angle of $\pi/2$ has $D = -1$, whereas highly flattened X-type (“sheet”) nulls have $D \approx 0$. We see from Figure 9 that the nulls in the pre-breakout phase are very low degree “sheet nulls”, which are too small to be visible in the global images (e.g., Fig. 3 and associated movie). These nulls induce negligible dynamics, and are likely due to a form of weak tearing. Even during this phase, the current sheet continues to lengthen and strengthen, implying that the tearing-associated

reconnection is insignificant. The local dynamics change significantly with the appearance of reconnection jets in the breakout sheet at $\sim 62,000$ s, although this is barely reflected in the globally integrated kinetic energy shown in Figure 4. The character of the nulls also changes shortly after this time (Fig. 9): the X-type nulls evolve from all sheet nulls to a broader range dominated by nulls with substantial opening angles, indicating the transition from a quasi-smooth sheet to a more broken structure containing distinct magnetic islands formed by reconnection. The degree distribution for O-points after 60,000 s is similar to that of the X-points shown in Figure 9. The appearance of high-degree nulls and reconnection jets is accompanied by a clear increase in the rate of flux transfer from the core (blue flux in Fig. 1) to the lobes, signaling the onset of fast reconnection.

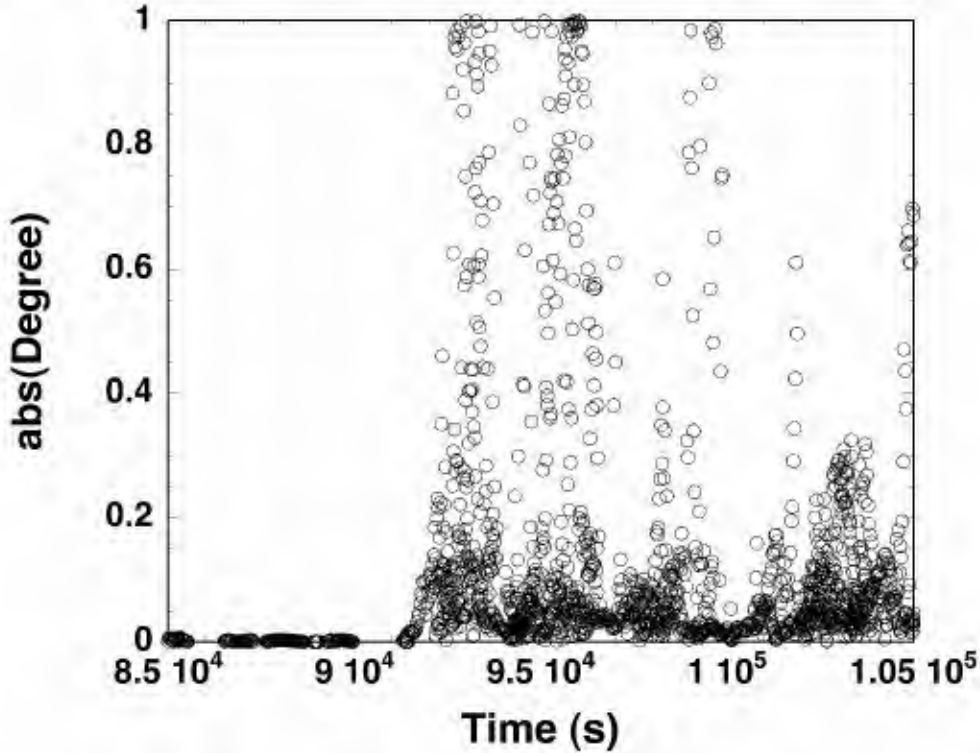


Figure 10. Absolute value of degree D (see Appendix) of X-type nulls in the flare current sheet before and during the early impulsive phase. Each black circle at a specific time represents an individual null.

Another important topological change begins during the breakout-driven phase, at around 82,575 s: the first X- and O-type nulls appear in the flare current sheet (Fig. 8).

Again the nulls initially have low degree (Fig. 10), consistent with the formation of magnetic islands as a result of weak tearing rather than strongly driven reconnection.

Using the null finder described in the Appendix, we followed the nulls in the flare current sheet and found that most propagate downward slowly. This intriguing phenomenon was not seen in our previous lower-resolution simulations. The motions become obvious when the individual nulls in the flare sheet are tracked, as depicted in Figure 11. Prior to the onset of reconnection jets in the flare sheet, four islands were detected; one disappeared quickly but the other three traveled downward at speeds ranging from 20 to 80 km s⁻¹. This phenomenon is possibly related to the descending loop-top sources reported for several high-energy flares (e.g., Sui & Holman 2003; Sui et al. 2004, 2006; Joshi et al. 2007); however, our model cannot predict what X-ray signatures might be associated with these descending nulls.

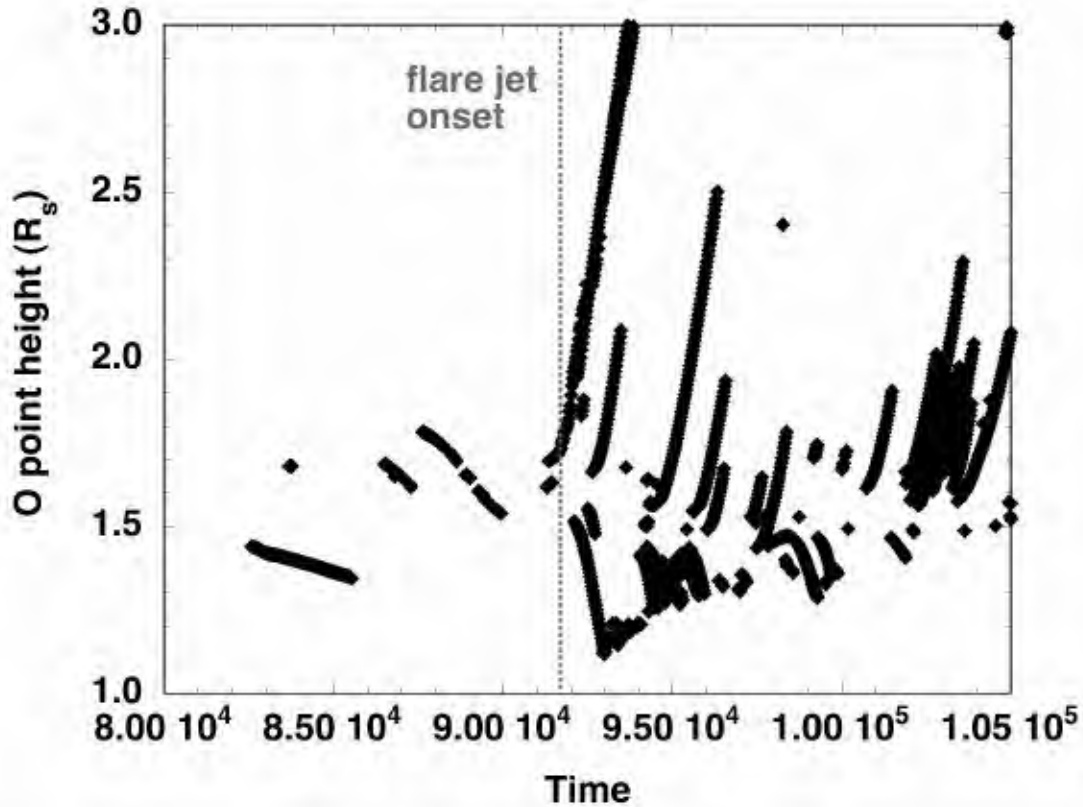


Figure 11. Height vs. time of O-type nulls at 25-s intervals during the breakout-driven and explosive phases. The O point that originated around $1.7R_s$ shortly before jet onset became the axis of the CME flux rope, and rose beyond the heights shown here (see Fig. 15).

3.3 The Explosive Eruption Phase

The breakout-driven eruptive phase ends at $\sim 91,700$ s with the onset of strong reconnection at the flare current sheet, signaled by the appearance of reconnection jets there and the sharp upturn in integrated kinetic energy seen in Figure 4. This time also marks the start of the formation of the highly twisted flux rope that comprises the CME (see Fig. 12). Note that the erupting flux is still a sheared arcade before the onset of flare reconnection. In the breakout model, as in the other reconnection-driven models, the ejected flux rope (whose central O-type null is tracked in Fig. 11) forms *as a result* of eruption.

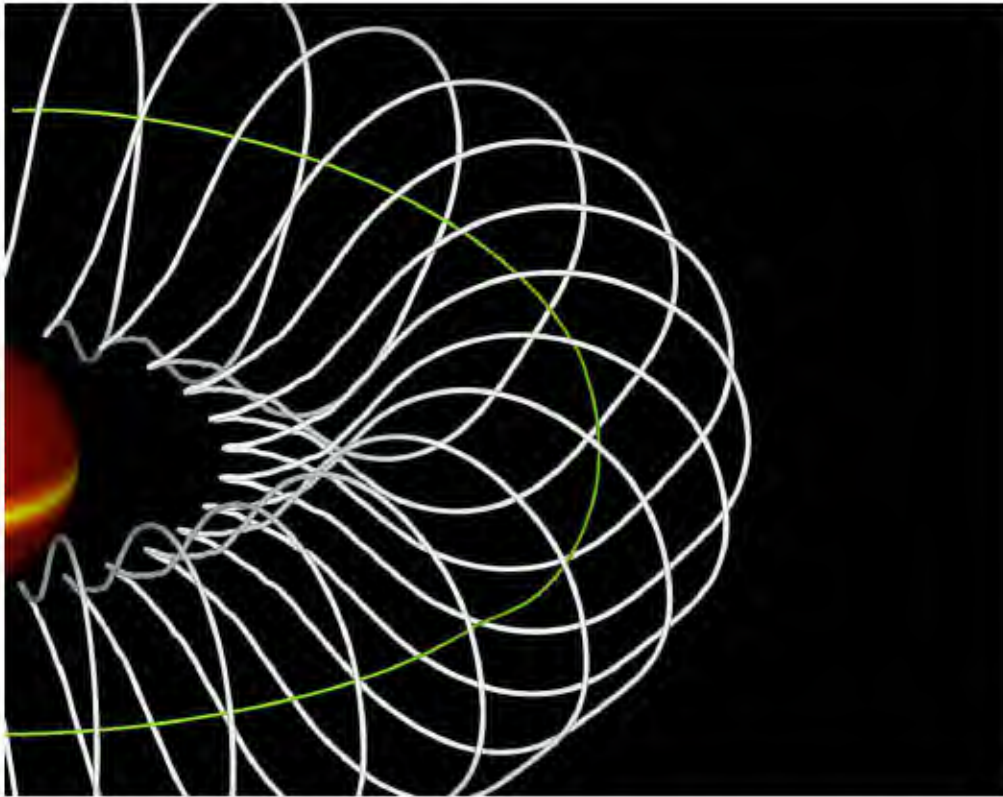


Figure 12. Outermost field line (white) and axis (green) of the CME flux rope created by flare reconnection, at $t=100,000$ s. The solar surface coloring is the same as in previous figures.

A distinct change in the flare reconnection dynamics occurs at 91,700 s. Up to this time the flare current sheet continues to lengthen, even while undergoing island formation, reaching an aspect ratio (length to width) of ~ 220 . This value far exceeds the threshold for tearing instability in an equilibrium current sheet (e.g., Furth et al. 1963); however, our system is not in equilibrium but strongly driven. The current sheet begins to

shrink only when the reconnection transitions from slow tearing to its strongly dynamic form that includes Alfvénic jets.

As with the breakout sheet, the shape of the nulls also changes at fast reconnection onset. Figure 10 shows that all nulls in the flare current sheet prior to 91,700 s are highly flattened sheet nulls of low degree, but afterwards the range increases to the maximum possible. In addition, the velocities of the nulls increase up to the Alfvén speed and include both upward and downward directed motions (Fig. 11).

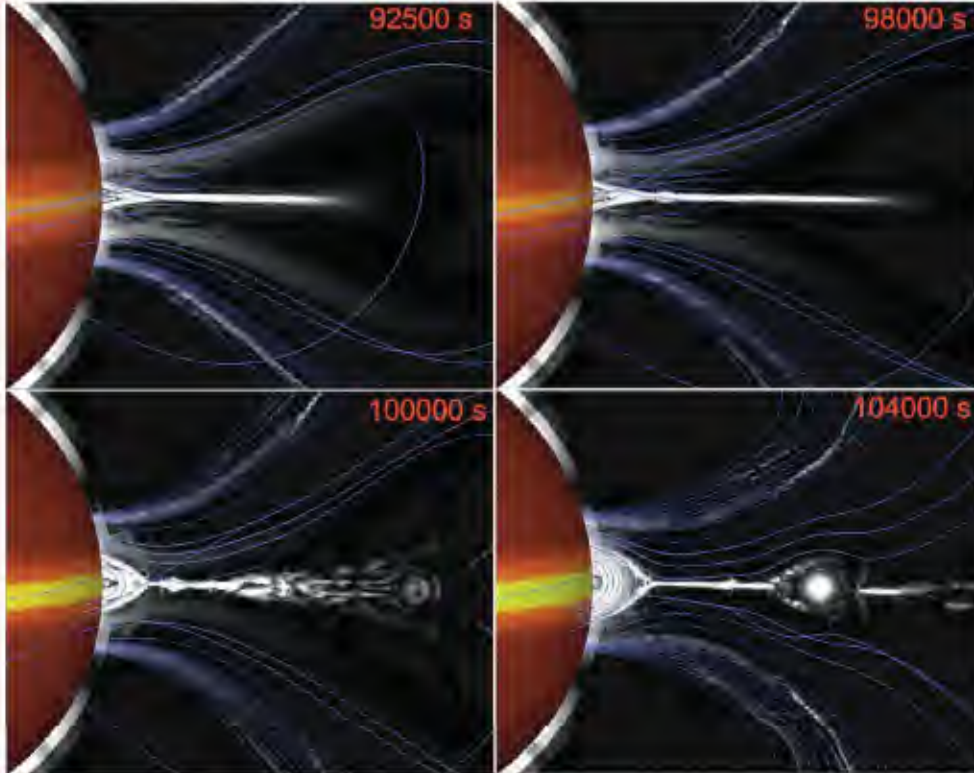


Figure 13. Close-up view of photospheric B_ϕ (red/yellow contours on the solar surface), normalized current density $R_\phi|J|/c$ in the r - θ plane (grayscale), and magnetic field lines (blue) in the simulation during the impulsive flare phase. The frame-to-frame variations in B_ϕ on the solar surface are explained in the first discussion of Fig. 3. The temporal evolution is shown in the movie available in the electronic edition (movie2.mpg). As in Fig. 3, the minimum B_ϕ (dark red) is zero; the maximum value (yellow) is saturated at 2 G. The minimum value of $R_\phi|J|/c$ (black) is effectively zero; the maximum (white) is saturated at 0.2 G.

The detailed dynamics of the flare sheet and vicinity during the strongest reconnection are shown in Figure 13 and its accompanying movie (movie2.mpg). Magnetic islands intermittently form and are ejected from the top of the flare sheet, contributing to the highly complex current structure at the back of the CME (Figs. 3 and 13). Throughout this time other islands travel downward, ultimately reconnecting with and adding flux to

the flare loops (Figs. 3 and 13). Curved external shocks emanate from the flanks of each new island, and travel up or down with the island. The creation of multiple islands and the reflection of the downward-moving shocks at the solar surface, which are most visible in the movie accompanying Figure 13, increase the complexity and fine structure of the current density within and around the flare sheet, creating a region of quasi-turbulent dynamics.

The number of islands in each current sheet and in the flux rope itself (which must contain at least one O-type null) fluctuates substantially from breakout onset through the rest of the simulation, as shown in Figure 8. The first small peak/plateau in the breakout-sheet null count during the impulsive phase, around 95,000-100,000 s, coincides with the only peak in the flux rope null count. The maximum number of nulls occurs around 115,000 s in both flare and breakout current sheets, while a secondary peak in both cases appears at $\sim 135,000$ s. However, the null counts in both sheets appear largely uncorrelated at other intervals, e.g., between 100,000 and 110,000 s.

To determine the relationship between flare and breakout nulls quantitatively, a cross-correlation was performed separately for the number of X- and O-type nulls in the breakout and flare current sheets, using the C_CORRELATE program in IDL. For X-points, the peak cross-correlation function value is ~ 0.84 at a lag time of $\sim 6,500$ s, slightly exceeding the simultaneous (zero lag time) correlation value, and the characteristic decorrelation time (i.e., the e-folding width) is $\sim 14,000$ s. The finite lag time at peak correlation is consistent with the delay between the onset of strong breakout reconnection around 75,000 s (as indicated by the number of nulls) and the onset of weak flare reconnection. O-points exhibit similar behavior but the correlation function maximum is slightly lower (0.81). These measures confirm that the instantaneous numbers of nulls in the two current sheets are strongly but imperfectly correlated, verifying that there is significant feedback between the breakout and flare reconnection.

The continual formation and ejection of islands in both breakout and flare current sheets implies that islands are an essential feature of fast reconnection in our simulations, in agreement with many other reconnection studies (e.g., Biskamp 1986; Drake et al. 2006; Daughton et al. 2009; Fermo et al. 2010). We calculated the flare reconnection rate ξ at selected times between 95,000 s and 105,000 s by taking the ratio of the inflow speed

to the outflow speed associated with the dominant X-type null in the current sheet (i.e., the origin of both reconnection jets). We found that $\xi \approx 0.09$ at all sampled times, although the large spatial variation of the outflow velocities (due to the presence of multiple islands) yields large uncertainties. This estimate is consistent with the rate predicted by several models for fast quasi-steady reconnection (e.g., Shay et al. 1999; Priest & Forbes 2000).

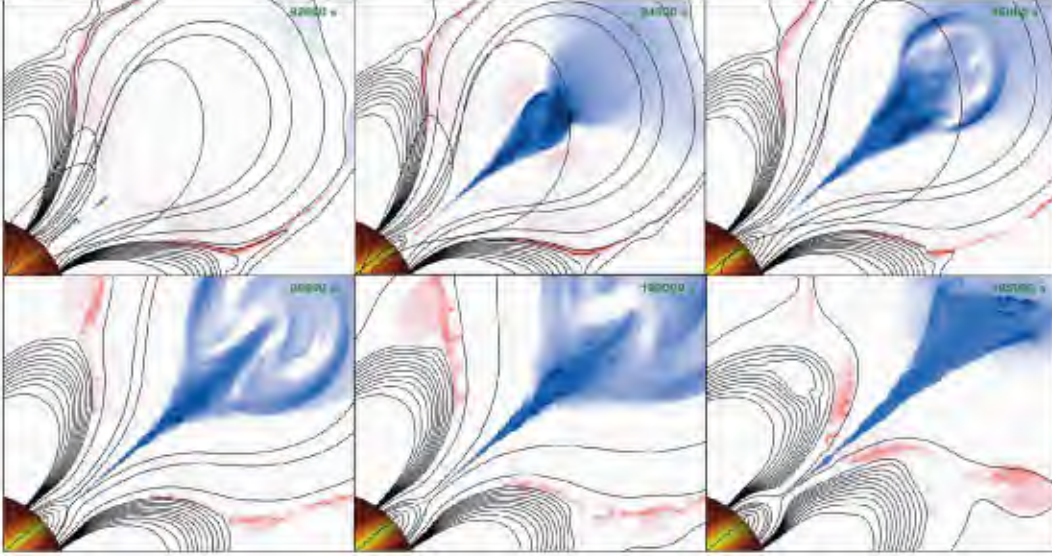


Figure 14. Close-up view of the radial velocity v_r at selected times during the impulsive flare phase. Red indicates downflows, while blue indicates upflows; both are saturated at $|v_r| = 500 \text{ km s}^{-1}$ for greater visibility of the slower motions. Selected field lines are shown in black; solar surface coloring is the same as in previous figures. See accompanying movie3.mpg in the electronic version for more details.

In addition to the islands, a characteristic feature of fast reconnection is the appearance of fast reconnection jets at the ends of the current sheet, as clearly evident in Figure 14 and the accompanying movie (movie3.mpg). The upper reconnection jet widens and becomes elongated quickly, reaching the flux rope axis by $\sim 93,000$ s. At roughly the same time the lower jet stops extending and the downward-directed kinetic energy saturates. Thereafter the lower jet terminates at progressively greater heights as the flare loop arcade grows. This shrinkage of the downward jet is tracked by the final location of the downward-directed nulls in Figure 11, indicating that the maximum extent of the lower jet is approximately $0.4 R_s$ at $\sim 93,000$ s. Figure 11 also shows that the main reconnection site between the two jets ends up near its initial location late in the explosive phase, indicating that the height of the reconnection varies little throughout the event although the flare arcades form at progressively larger heights. The largest islands,

on the other hand, originate progressively lower in the atmosphere, from $\sim 1.7 R_s$ at flare jet onset to $1.5 R_s$ at CME front take-off.

Although the jets are fast, they are not super-Alfvénic. At 91,500 s, $v_A \approx 300\text{--}500 \text{ km s}^{-1}$ where the lower jet will be located and $500\text{--}800 \text{ km s}^{-1}$ where the upper jet will appear. In comparison, at $t=92,500 \text{ s}$ the lower jet speeds range from $100\text{--}400 \text{ km s}^{-1}$ while the upper jet speeds range from $100\text{--}600 \text{ km s}^{-1}$. This upper jet introduces complicated fine structure into the core of the rising flux rope through the accumulation and expulsion of multiple islands from the current sheet that are then swept up in the flow, and through the destabilization of the interface between the jet and its surroundings by Kelvin-Helmholtz-like MHD instabilities (Fig. 14). The density in the upper jet is approximately an order of magnitude greater than in the surrounding plasma, while B_ϕ is reduced by a factor of 3 within the core of the jet compared with external conditions, indicating approximate pressure balance between the jet and its surroundings.

The relative timing between the flare and the associated CME has long been recognized as a fundamental indicator of their physical relationship. Consequently, numerous observational studies have been dedicated to measuring this important property (e.g., Harrison 1995; Zhang et al. 2001, 2004; Qiu et al. 2004; Temmer et al. 2008, 2010), which can be used to test predictions of solar eruption models. In the breakout model this timing is easily understood. The CME does begin first, as is evident from the significant increase in upward velocity in Figure 5, but the eruption velocity is slow. This slow eruption stretches the core field lines to the point that a vertical current sheet forms and fast reconnection sets in. The first truly explosive energy release begins with the fast flare reconnection, which creates simultaneously the flare loops, the reconnection jets, and the CME flux rope. All fully-eruptive breakout calculations to date (e.g., MacNeice et al. 2004; Lynch et al. 2008; van der Holst et al. 2009) agree on this point, and find that fast CME acceleration and flare reconnection onsets are close in time, but the precise relationship between flare and CME is not clear from these papers. The current study was deliberately designed to settle this issue.

The key point is that the impulsive flare and the energized CME flux rope are formed by a single reconnection process, and hence are physically simultaneous. This is a critical

observational distinction between the breakout model and ideal models based on kink or torus instability (e.g., Török & Kliem 2005). For at least some ideal models we expect the CME to accelerate to Alfvénic speeds appreciably *before* flare onset. In contrast, a recent analysis of EUV images and hard X-ray emission from 37 fast eruptive events confirms the tight coupling predicted by our model (Berkebile-Stoiser et al. 2012).

The partitioning of energy in eruptive events – that is, the amount of energy directed downward into the flare versus the amount directed upward into the CME – also offers critical insight into the physical processes governing the CME-flare relationship, and thus provides an important basis for evaluating closure between theory and observations. Our model-based estimates are not fully definitive because the simulation does not include kinetic effects and particle acceleration. Nevertheless, we can get an indication of the balance between flare and CME by examining the kinetic energies of the upward and downward flare-reconnection jets. At the very beginning of the jets’ existence, the downflows are twice as fast as the upflows ($v_r \approx -120$ vs. 60 km s^{-1}), but thereafter the maximum upflows are stronger than the downflows by as much as a factor of 2, implying that approximately twice as much energy goes into the CME as into the flare. This result is consistent with studies of the energetics of fast CMEs/eruptive flares (e.g., Webb et al. 1980; Emslie et al. 2004).

As in an actual event, the speed and acceleration of the CME in our simulation depends on exactly where one measures the evolution. In broad terms, one can consider the eruption to be driven by two main forces: the direct impulse imparted by the upward reconnection jet, and the magnetic buoyancy of the disconnected CME plasmoid. The velocity of the upward jet sets the initial speed of the flux rope for roughly 1 hr after flaring begins. We find that the flux rope axis rises at $\sim 460 \text{ km s}^{-1}$ until $\sim 95,000 \text{ s}$, then slows down to $\sim 150 \text{ km s}^{-1}$ when the axis rises beyond the direct influence of the jet, and the flux rope becomes sufficiently large to be identifiable as a CME (see Fig. 15). We can now explain why the sharp rise in integrated kinetic energy (Fig. 4) is not simultaneous with the CME front take off. The integrated kinetic energy is dominated first by the jet flows caused by the retraction of the newly reconnected field upward, which do not immediately affect the plasma closer to the breakout sheet. When the jet has transported the first-formed island to the CME core, where the flow stagnates and develops

complex structure, the CME gains sufficient momentum and energy, and the restraining tension becomes sufficiently low, to enable fast acceleration of the CME.

The magnetic buoyancy of the CME is responsible for the bulk of the mass acceleration, but it does not become dominant until the plasmoid has grown to global size. As shown in Figure 15, CME front “take-off” occurs at $t \approx 95,000$ s, well after the onset of reconnection in the flare current sheet. Thereafter the CME front accelerates to $\sim 360 \text{ km s}^{-1}$, comparable to the local Alfvén speed, and remains at that speed until the end of the run. The flux rope axis, however, lags behind the CME: it accelerates again around $105,000$ s from ~ 150 to $\sim 260 \text{ km s}^{-1}$, remaining at that speed thereafter. This expected disparity in speed between the cavity front and the flux-rope axis follows directly from the expansion that is inherent to the evolution of a global structure such as a CME. However, the key point remains that the flare impulsive phase and the CME strong-acceleration phase have the same physical origin: the onset of fast flare reconnection.

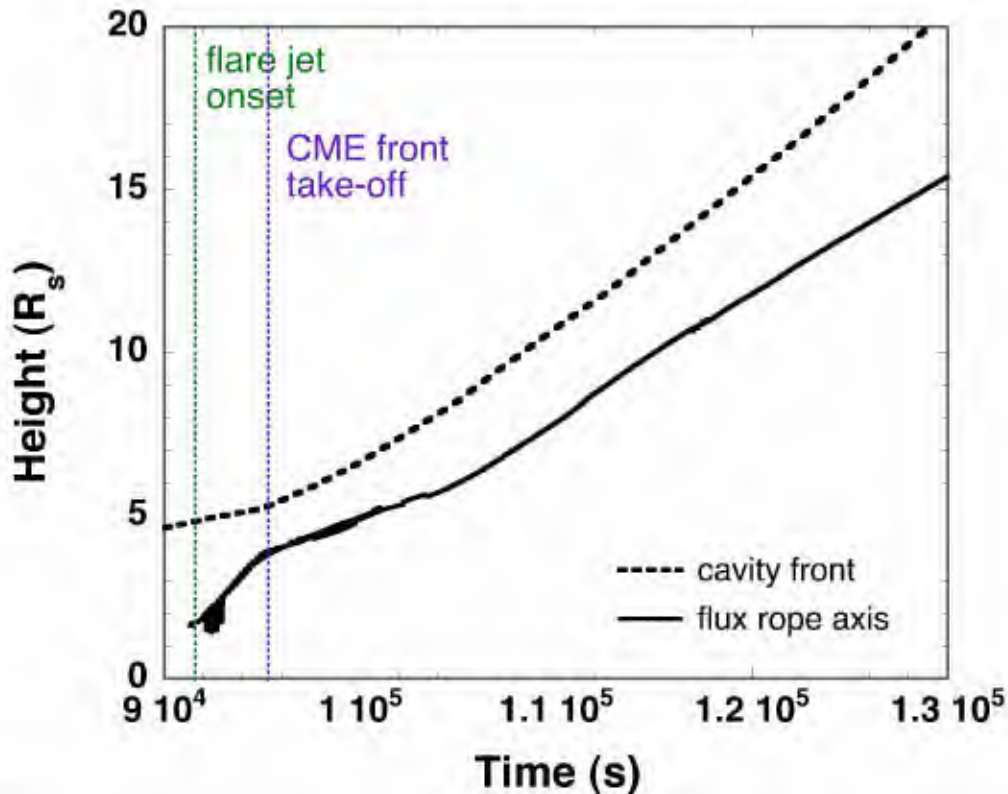


Figure 15. Height of the cavity front and flux rope axis vs. time. Here the front is defined as the location where the mass density increases sharply behind the breakout current sheet, and the flux rope axis is an O-type null. A thicker track is shown in certain intervals before $\sim 102,000$ s because two O-type nulls exist in the flux rope at those times.

4. Discussion

4.1 The Eruption Mechanism

The results described above demonstrate that the trigger for the explosive energy release and ejection is the onset of fast reconnection in the flare current sheet, essentially a resistive instability. This conclusion requires verification, however, because the buildup of the CME plasmoid may trigger instead an ideal instability or a loss of equilibrium, which could produce the observed late-stage acceleration. We can distinguish between ideal and resistive mechanisms by calculating the energy required for an ideal eruption and comparing it to the actual system energy. Note that, for an ideal ejection, the system's magnetic energy must exceed the magnetic energy of the appropriate partially open configuration as described in DeVore & Antiochos (2005). If the energy of this partially open state is less than or equal to the simulation magnetic energy at take-off, then the physical mechanism is likely a loss of equilibrium or ideal instability; if the partially open energy is higher, then additional reconnection is needed for eruption, so the mechanism is inherently a resistive instability.

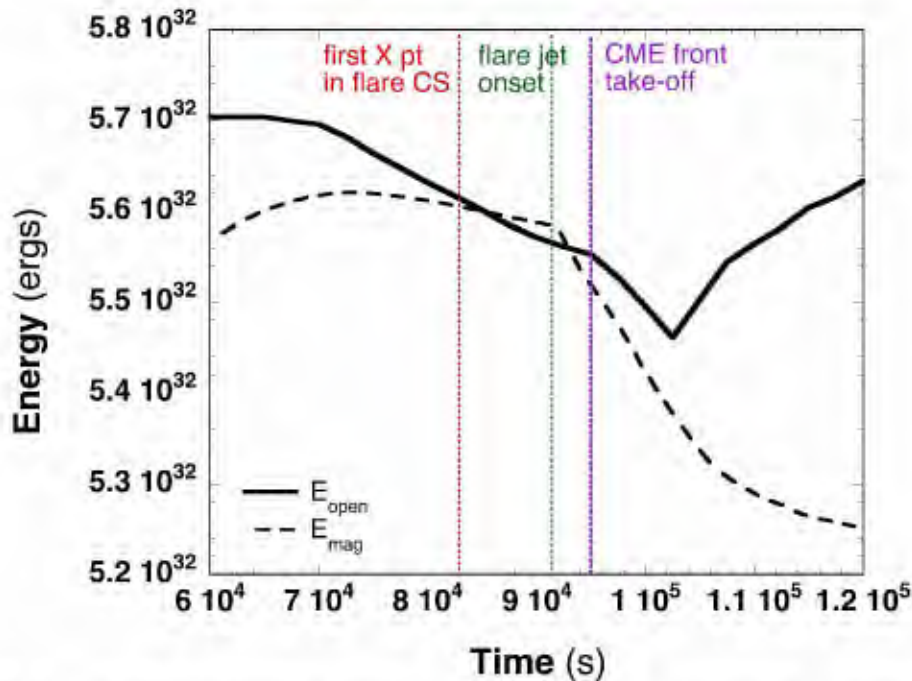


Figure 16. Volume-integrated magnetic energy (E_{mag}) and partially open energy (E_{open}) in the middle of the breakout simulation. Key times are marked by dotted vertical colored lines

We have determined the energy of the relevant partially open magnetic field, E_{open} , at 2500-s intervals throughout the calculation (solid line in Fig. 16), using the same procedures employed to create Figure 4 of DeVore & Antiochos (2005). The partially open energy is set by the location of the separatrix between the two side flux systems and the inner and outer systems. As breakout reconnection proceeds and flux is transferred from the inner and outer systems to the sides, this separatrix moves inward (Fig. 1). Because only the inner and outer flux systems must open to eject the sheared flux, the open energy decreases as shown in Figure 16. At later times, the flare reconnection transfers enough flux back into the inner and outer systems that the open energy starts to increase, but this occurs well into the explosive phase.

Figure 16 shows the time evolution of E_{open} along with that of the volume-integrated magnetic energy in the computational domain, E_{mag} (dashed line in Fig. 4). Early in the evolution, the open energy is well above the actual system energy, so there is no possibility for an ideal eruption. The total magnetic energy reaches its peak around 73,250 s and then decreases slowly until flare jet onset, but the open energy E_{open} drops steadily throughout that time until it falls below E_{mag} at $\sim 85,700$ s. It is possible that the system loses ideal stability at this time, but there is no evidence for a significant change in the dynamics; the system continues to undergo a slow eruption consistent with breakout reconnection. The difference between these energies grows and reaches a maximum $\sim 2 \times 10^{30}$ ergs, at a time approximately coincident with flare jet onset. Again there is no evidence for an explosive ideal eruption at this time, even though the magnetic energy stored in the system is more than sufficient to eject the sheared flux to the heliosphere. In fact, the CME front doesn't begin its fast "take-off" until later, when the system energy has dropped back below the open energy. We conclude that the explosive ejection seen in this 2.5D simulation is caused by reconnection, i.e., a resistive instability rather than an ideal process.

4.2 Scaling to Observed Events

In order to compare the results of our simulation to observed CME/eruptive flares, we must scale the parameters of our model to those of an active region on the Sun. There are

two critical parameters: the typical length scale of the event and the typical time scale. The length scale is determined by the size of the active region that produces the event. For a large set of CME/flare producing active regions, the average active-region pole separation is $\langle d_{\text{obs}} \rangle \sim 92$ Mm (D. Falconer, personal communication; see also Falconer et al. 2002), whereas the corresponding value for our model is $\langle d_{\text{sim}} \rangle \sim 1100$ Mm (angular separation of 45°). Consequently, our active region is approximately an order of magnitude larger than true solar active regions. We chose such a large scale for the simulated active region simply to maximize the spatial resolution of the calculation, which is especially important when performing grid-scaling studies.

The time scale is set by the Alfvén crossing time of the active region (the ratio of the length scale to the Alfvén speed). For typical solar active regions, $V_A \sim 2,000$ km s⁻¹, whereas for our system the Alfvén speed in the inner core of the region is closer to 500 km s⁻¹. Comparing the ratios $V_A/\langle d \rangle$ implies a factor of ~ 40 difference in time scales between our system and the Sun.

By applying this temporal normalization factor to our results, we find that the interval between the first appearance of islands in the breakout sheet and the first X-type null in the flare sheet scales down to ~ 600 s, the onset of reconnection jets takes place ~ 200 s after the appearance of the first null in the flare sheet, and the delay between the flare jet onset and the CME front take-off is reduced to ~ 70 s. If the impulsive phase of observed flares is associated with the interval during which the strongly sheared core flux undergoes flare reconnection in our simulation, then the main impulsive phase lasts about 7,000 s in our simulation, which would correspond to ~ 180 s for a typical active region. Alternatively, if one signature of flare impulsiveness is the existence of numerous nulls in the flare sheet, then the impulsive phase would last somewhat longer, $\sim 32,500$ s of simulation time or ~ 800 s for a real active-region event. These timescales are consistent with most impulsive-phase observations (see, e.g., Krucker et al. 2008; Hudson 2011).

Using the length normalization described above, we also scale the upward and downward displacements of the nulls in the flare sheet (Fig. 11) to active region dimensions. The downward shift in position of the main reconnection site in the flare sheet during the peak impulsive phase becomes $\sim 15,900$ km ($22''$); a comparable displacement is seen for the longest-lived sheet null observed during the preflare phase.

The estimated increase in the height of the uppermost post-eruption arcade top between 93,000 and 105,000 s is of order 23,500 km (33''), comparable to the maximum length of the lower jet at the start of that interval. These numbers also are consistent with typical solar flare observations.

This agreement between the scaled simulation results and actual CME/flare parameters should not be interpreted as independent verification of the model. The only real test of the model is that our simulation does produce an Alfvénic ejection that evolves consistent with the sequence of events generally observed in a fast CME/eruptive flare.

5. Conclusions

The results presented in §§3 and 4 lead to several important conclusions on the origins and dynamics of CMEs/eruptive flares, and on the nature of reconnection in the solar corona. First, we conclude that the onset mechanism for eruption is the start of fast reconnection between the inner flux system containing the filament channel and external surrounding flux systems. Once this breakout reconnection begins, the force balance between the upward magnetic pressure of sheared filament-channel flux and the magnetic tension of overlying near-potential flux is permanently destroyed. As a result, the outward expansion of the sheared flux accelerates and never slows down. Here we considered a system with significant symmetry, so this breakout reconnection was centered above the erupting flux system. However, the same basic mechanism works as well when the null point is off to one side and/or the system is fully 3D (e.g., Roussev et al. 2007; Lynch et al. 2008, 2009; van der Holst et al. 2009; Masson et al. 2012).

Based on our results, if one could observe the onset of fast breakout reconnection, one could predict with certainty that a CME/flare will occur. Unfortunately, the lead time is not very long. We found (§3) that fast breakout reconnection began at $\sim 60,000$ s and fast flare reconnection at $\sim 90,000$ s; scaling to solar active-region parameters (§4.2) implies a time difference of only tens of minutes. In fact, we observed a comparable interval between breakout onset and flare onset in the 14 July 1998 event (Aulanier et al. 2000). Therefore, it appears unlikely that we will be able to predict accurately the occurrence of

a breakout CME days in advance; on the other hand, even tens of minutes may prove helpful.

We also conclude that the mechanisms for impulsive CME acceleration and for impulsive flare energy release are one and the same: the onset of fast reconnection at the flare current sheet. A single process, flare reconnection, is responsible for the bulk of the energy release, whether into mass motions, heating, or particle acceleration. Furthermore, we find that the physical mechanism for eruption in the breakout model is a resistive instability, as in a resistive kink, and not an ideal instability/loss of equilibrium (Fig. 16). It should be possible to test the validity of this result against well-observed solar events by precise measurement of the relative timing between impulsive flare onset and CME acceleration.

An important question is, how does our model explain CMEs that show negligible flare emission? We find that eruption will occur even without flare reconnection, but the eruption will be slow, more like a streamer blowout (e.g., Sheeley et al. 1997) than a fast CME. Therefore we predict a clear difference in the early acceleration profile between CMEs with and without impulsive flares, although the final velocity of any CME clearly depends on the solar wind speed.

Flare reconnection plays the central role in our model because it is the primary process for relaxing the magnetic field back down toward its minimum-energy closed state. Our results imply, therefore, that accurate calculations of flare reconnection are absolutely essential for understanding and predicting CME/flare onset and development. Unfortunately, such calculations will be highly challenging, because flare reconnection inherently involves coupling from the global scales at which the current sheet is driven to the kinetic scales at which it is disrupted. This coupling across scales is clearly evident in our simulations, and is their most intriguing feature. We find that the global dynamics are closely tied to the dynamics at the grid scale where the flux breaking occurs. In the actual corona the range between the global and the flux-breaking scales is much larger than in our simulation, but we still expect the same type of multiscale coupling to dominate the dynamics. The fact that so much of the flare energy is often inferred to reside in energetic particles (Miller et al. 1997; Emslie et al. 2004; Holman et al. 2011), which must be

accelerated by kinetic processes, is compelling additional evidence for this multiscale coupling.

Another major conclusion concerns the fundamental nature of coronal reconnection. As we have argued repeatedly, it is not possible to separate reconnection from the current-sheet formation process. Two distinct current sheets form in our simulation through two very different, well-known mechanisms: the stressing of a null point as described by Syrovatskii (1981), and the stretching of dipolar field lines into a near-open configuration as in the formation of the heliospheric current sheet or the magnetotail. In both cases the current sheet forms slowly, well below the Alfvén speed, and extends to large aspect ratios, well above 100. This pattern of behavior is likely to be an essential property of all reconnection: for the width of a current sheet to decrease down to the flux-breaking scale through ideal evolution, the current sheet length invariably must extend to global scales. Consequently, we expect that all current sheets will have large aspect ratios at the onset of reconnection, so this early reconnection will likely be a form of tearing that creates plasmoids. Note that the evolution of the sheet *after* reconnection onset, whether it maintains a global length scale and continues plasmoid formation or shrinks to a Petschek-type configuration (or develops some other structure), will be controlled by the reconnection itself, which depends on the flux-breaking mechanism. Therefore, the structure and dynamics of coronal current sheets are determined by the interplay between the global ideal stressing that creates the sheet and the local kinetic reconnection that destroys it.

That interplay is especially evident in the flare current sheet of our simulation. The sheet clearly grows to global scales before reconnection starts, but this initial reconnection appears to be a slow tearing that cannot keep pace with the current-sheet formation process. However, the slow reconnection eventually transitions to a fast form with strong collimated Alfvénic jets. In its fast form the reconnection achieves a rate of $\sim 10\% V_A$, which is sufficient to account for the rapid energy release characteristic of observed CMEs/flares (e.g., Yokoyama et al. 2001; Jing et al. 2005; Takasao et al. 2012). The reason for the transition to fast reconnection can be deduced from Figure 11, which shows the evolution of the magnetic islands that form in the flare current sheet. Note that flare jet onset occurs soon after the appearance of the first O-type null that moves upward

and eventually becomes the axis of the CME. An island moving upward stretches the immediately overlying flux; this flux is forced to reconnect behind the plasmoid, thereby adding flux to the plasmoid and accelerating the upward motion. This feedback process is physically similar to the feedback in the breakout reconnection, except that it releases much more energy and leads to explosive dynamics. It is the process underlying the resistive instability discussed above.

The most surprising feature of our simulation is that this instability does not turn on as soon as reconnection begins in the flare current sheet. As shown in Figure 11, the first few islands that form in the flare current sheet move *downward* rather than upward. Downward moving islands have essentially nowhere to go. They can only merge back into the flux from which they originated, thus releasing little energy, unless they move at much higher speeds than are evident in Figure 11. We are still working to understand the exact reasons for this delay between the onset of reconnection and the onset of upward moving islands. However, this delay clearly is related to the nature of the global-local coupling that underlies all major explosive activity observed in the Sun's atmosphere.

6. Acknowledgements

We thank B. Dennis, D. Falconer, and K. D. Leka for helpful discussions, and the referee for suggestions that have improved this paper. This work was supported in part by NASA's LWS and Heliophysics SR&T research programs. The computer resources were provided by the DoD HPCMP.

References

- Alexander, D., Liu, R., & Gilbert, H. R. 2006, *ApJ*, 653, 719
- Amari, T., Luciani, J. F., Mikić, Z., & Linker, J. A. 2000, *ApJ*, 529, L49
- Antiochos, S. K. 1990, *J. Italian Astron. Soc.*, 61, 369
- Antiochos, S. K. 1998, *ApJ*, 502, L181
- Antiochos, S. K., Dahlburg, R. B., & Klimchuk, J. A. 1994, *ApJ*, 420, L41
- Antiochos, S. K., DeVore, C. R., & Klimchuk, J. A. 1999, *ApJ*, 510, 485
- Arnol'd, V. I. 1992, *Ordinary Differential Equations*, 3rd edition, trans. R. Cooke (New York: Springer)
- Aulanier, G., DeLuca, E. E., Antiochos, S. K., McMullen, R. A., & Golub, L. 2000, *ApJ*, 540, 1126
- Aurass, H., Mann, G., Zlobec, P., & Karlický, M. 2011, *ApJ*, 730, 57
- Berkebile-Stoiser, S., Veronig, A. M., Bein, B. M., & Temmer, M. 2012, *ApJ*, 753, 88
- Bhattacharjee, A., Huang, Y.-M., Yang, H., & Rogers, B. 2009, *Phys. Plasmas*, 16, 112102, doi:10.1063/1.3264103
- Biskamp, D. 1986, *Phys. Fluids* 29, 1520
- Cheng, X., Ding, M. D., & Zhang, J. 2010, *ApJ*, 712, 1302
- Cook, G. R., Mackay, D. H., & Nandy, D. 2009, *ApJ*, 704, 1021
- Daughton, W., Roytershteyn, V., Albright, B. J., Karimabadi, H., Yin, L., & Bowers, K. J. 2009, *Phys. Rev. Lett.*, 103, 065004
- Deng, N., Liu, C., Yang, G., Wang, H., & Decker, C. 2005, *ApJ*, 623, 1195
- DeVore, C. R. 1991, *J. Comput. Phys.*, 92, 142
- DeVore, C. R. & Antiochos, S. K. 2005, *ApJ*, 638, 1031
- DeVore, C. R. & Antiochos, S. K. 2008, *ApJ*, 680, 740
- DeVore, C. R., Antiochos, S. K., & Aulanier, G. 2005, *ApJ*, 629, 1122
- Drake, J. F., Swisdak, M., Schoeffler, K. M., Rogers, B. N., & Kobayashi, S. 2006, *Geophys. Res. Lett.*, 33, L13105, doi:10.1029/2006GL025957
- Emslie, A. G., et al. 2004, *J. Geophys. Res.*, 109, 10104
- Falconer, D. A., Moore, R. L., & Gary, G. A. 2002, *ApJ*, 569, 1016
- Fang, F., Manchester, W. IV, Abnett, W. P., & van der Holst, B. 2012, *ApJ*, 745, 37
- Fermo, R. L., Drake, J. F., & Swisdak, M. 2010, *Phys. Plasmas*, 17, 702
- Forbes, T. G. & Isenberg, P. A. 1991, *ApJ*, 373, 294
- Forbes, T. G., et al. 2006, *Space Sci. Rev.*, 123, 251
- Furth, H. P., Killeen, J., & Rosenbluth, M. N. 1963, *Phys. Fluids*, 6, 459
- Gaizauskas, V. 2001, in *Encyclopedia of Astronomy and Astrophysics*, ed. P. Murdin (Philadelphia: Nature)
- Gary, G. A., & Moore, R. L. 2004, *ApJ*, 611, 545
- Greene, J. M. 1992, *J. Comput. Phys.*, 98, 194
- Harrison, R. A. 1995, *A&A*, 304, 585
- Haynes, A. L. & Parnell, C. E. 2007, *Phys. Plasmas*, 14, 082107
- Hindman, B. W., Haber, D. A., & Toomre, J. 2006, *ApJ*, 653, 725
- Holman, G. D., et al. 2011, *Space Sci. Rev.*, 159, 107
- Hudson, H. S. 2011, *Space Sci. Rev.*, 158, 5
- Jacobs, C., Roussev, I. I., Lugaz, N., & Poedts, S. 2009, *ApJ*, 695, L171
- Jing, J., Qiu, J., Lin, J., Qu, M., Xu, Y., & Wang, H. 2005, *ApJ*, 620, 1085

- Joshi, B., Manoharan, P. K., Veronig, A. M. & Pandey, K. 2007, *Sol. Phys.*, 242, 143
- Kazachenko, M. D., Canfield, R. C., Longcope, D. W., Qiu, J., Des Jardins, A., & Nightingale, R. W. 2009, *ApJ*, 704, 1146
- Krucker, S., et al. 2008, *Astron. Astrophys. Rev.*, 16, 155
- Lau, Y-T. & Finn, J. M. 1990, *ApJ*, 350, 672
- Lin, C.-H., Gallagher, P. T., & Raftery, C. L. 2010, *A&A*, 516, 44
- Lynch, B. J., Antiochos, S. K., DeVore, C. R., Luhmann, J. G., & Zurbuchen, T. H. 2008, *ApJ* 683, 1192
- Lynch, B. J., Antiochos, S. K., DeVore, C. R., & Zurbuchen, T. H. 2005, in *Solar Wind 11* (ESA), p. 297
- Lynch, B. J., Antiochos, S. K., Li, Y., Luhmann, J. G., & DeVore, C. R. 2009, *ApJ*, 697, 1918
- Lynch, B. J., Antiochos, S. K., MacNeice, P. J., & Zurbuchen, T. H. 2004, *ApJ*, 617, 589
- Mackay, D. H., Karpen, J. T., Ballester, J. L., Schmieder, B., & Aulanier, G., 2010, *Space Sci. Rev.*, 151, 333
- MacNeice, P. J., Antiochos, S. K., Phillips, A., Spicer, D. S., DeVore, C. R., & Olson, K. 2004, *ApJ*, 614, 1028
- MacNeice, P. J., Olson, K. M., Mobarry, C., de Fainchtein, R., & Packer, C. 2000, *Comput. Phys. Commun.*, 126, 330
- Mandrini, C. H., Démoulin, P., Schmieder, B., DeLuca, E. E., Pariat, E., & Uddin, W. 2006, *Sol. Phys.*, 238, 293
- Manoharan, P. K. & Kundu, M. R. 2003, *ApJ*, 592, 597
- Martin, S. F. 1998, *Sol. Phys.*, 182, 107
- Masson, S., Antiochos, S. K., & DeVore, C. R. 2012, *ApJ*, submitted
- Miller, J. A. et al. 1997, *J. Geophys. Res.*, 102, 14631
- Moore, R. L., Sterling, A. C., Hudson, H. S., & Lemen, J. R. 2001, *ApJ*, 552, 833
- Parnell, C. E., Smith, J. M., Neukirch, T., & Priest, E. R. 1996, *Phys. Plasmas* 3, 759
- Phillips, A., MacNeice, P., & Antiochos, S. K. 2005, *ApJ*, 624, L129
- Priest, E. R. & Forbes, T. 2000, *Magnetic Reconnection: MHD Theory and Applications* (New York: Cambridge U. Press)
- Priest, E. R. & Titov, V. S. 1996, *Phil. Trans. R. Soc.*, 354, 2951
- Qiu, J., Wang, H., Cheng, C. Z., & Gary, D. E. 2004, *ApJ*, 604, 900
- Rachmeler, L. A., DeForest, C. E., & Kankelborg, C. C. 2009, *ApJ*, 693, 1431
- Rondi, S., Roudier, Th., Molodij, G., Bommier, V., Keil, S., Sütterlin, P., Malherbe, J. M., Meunier, N., Schmieder, B., & Maloney, P. 2007, *A&A*, 467, 1289
- Roussev, I. I., Lugaz, N., & Sokolov, I. 2007, *ApJ*, 668, L87
- Seaton, D. B., Mierla, M., Berghmans, D., Zhukov, A. N., & Dolla, L. 2011, *ApJ*, 727, L10
- Shay, M. A., Drake, J. F., & Rogers, B. N. 1999, *Geophys. Res. Lett.*, 26, 2163
- Sheeley, N. R. Jr., et al. 1975, *Sol. Phys.*, 40, 103
- Sheeley, N. R., Jr., et al. 1997, *ApJ*, 484, 472
- Soenen, A., Zuccarello, F. P., Jacobs, C., Poedts, S., Keppens, R., & van der Holst, B. 2009, *A&A*, 501, 1123
- Sterling, A. C. & Moore, R. L. 2001a, *J. Geophys. Res.*, 106, 25227
- Sterling, A. C. & Moore, R. L. 2001b, *ApJ*, 560, 1045
- Sterling, A. C. & Moore, R. L. 2004a, *ApJ*, 602, 1024

- Sterling, A. C. & Moore, R. L. 2004b, *ApJ*, 613, 1221
- Sturrock, P. A. 1989, *Sol. Phys.*, 121, 387
- Sui, L. & Holman, G. D. 2003, *ApJ*, 596, L251
- Sui, L., Holman, G. D., & Dennis, B. R. 2004, *ApJ*, 612, 546
- Sui, L., Holman, G. D., & Dennis, B. R. 2006, *ApJ*, 646, 605
- Syrovatskii, S. I. 1971, *Sov. Phys. JETP*, 33, 933
- Syrovatskii, S. I. 1978a, *Astrophys. Space Sci.*, 56, 3
- Syrovatskii, S. I. 1978b, *Sol. Phys.*, 58, 89
- Syrovatskii, S. I. 1981, *ARA&A*, 19, 163
- Takasao, S., Asai, A., Isobe, H., & Shibata, K. 2012, *ApJ*, 745, L6
- Temmer, M., Veronig, A. M., Vršnak, B., Rybák, J., Gömöry, P., Stoiser, S., & Maričić, D. 2008, *ApJ*, 673, L95
- Temmer, M., Veronig, A. M., Kontar, E. P., Krucker, S., & Vršnak, B. 2010, *ApJ*, 712, 1410
- Titov, V. S., Mikić, Z., Linker, J. A., & Lionello, R. 2008, *ApJ*, 675, 1614
- Török, T. & Kliem, B. 2005, *ApJ*, 630, L97
- Tousey, R., et al. 1973, *Sol. Phys.*, 33, 265
- Ugarte-Urra, I., Warren, H. P., & Winebarger, A. R. 2007, *ApJ*, 662, 1293
- van der Holst, B., Jacobs, C., & Poedts, S. 2007, *ApJ*, 671, L77
- van der Holst, B., Manchester, W. IV, Sokolov, I. V., Toth, G., Gombosi, T. I., DeZeeuw, D., & Cohen, O. 2009, *ApJ*, 693, 1178
- Webb, D. F., et al. 1980, in *Solar Flares*, ed. P. Sturrock (Colorado Assoc. Univ. Press)
- Williams, D. R., Török, T., Démoulin, P., van Driel-Gesztelyi, L., & Kliem, B. 2005, *ApJ*, 628, L163
- Yokoyama, T., Akita, K., Morimoto, T., Inoue, K., & Newmark, J. 2001, *ApJ*, 546, L69
- Zhang, J., Dere, K. P., Howard, R. A., Kundu, M. R., & White, S. M. 2001, *ApJ*, 559, 452
- Zhang, J., Dere, K. P., Howard, R. A., & Vourlidas, A. 2004, *ApJ*, 604, 420
- Zuccarello, F. P., Jacobs, C., Soenen, A., Poedts, S., van der Holst, B., & Zuccarello, F. 2009a, *A&A*, 507, 441
- Zuccarello, F. P., Romano, P., Farnik, F., Karlicky, M., Contarino, L., Battiato, V., Guglielmino, S. L., Comparato, M., & Ugarte-Urra, I. 2009b, *A&A*, 493, 629
- Zuccarello, F. P., Soenen, A., Poedts, S., Zuccarello, F., & Jacobs, C. 2008, *ApJ*, 689, L157

Appendix: Refinement Criteria and Null Point Identification

For this study, we exploited *ARMS'* adaptivity criteria that allow us to pinpoint where the grid should (and should not) refine and, hence, to control the effective resistivity as precisely as possible. In order to resolve selectively the most important current-carrying structures, we evaluate the dimensionless measure

$$c \equiv \frac{\left| \iint_S \nabla \times \mathbf{B} \cdot d\mathbf{a} \right|}{\oint_C |\mathbf{B} \cdot d\mathbf{l}|} = \frac{\left| \oint_C \mathbf{B} \cdot d\mathbf{l} \right|}{\oint_C |\mathbf{B} \cdot d\mathbf{l}|} = \frac{\left| \sum_{n=1}^i B_{t,n} l_n \right|}{\sum_{n=1}^i |B_{t,n} l_n|}.$$

The numerator is simply the magnitude of the electric current passing through the surface S bounded by the contour C , its equivalent after using Stokes' theorem, and its discrete analogue on the grid, where $B_{t,n}$ is the tangential component of \mathbf{B} along the n th segment l_n of the contour C ; the denominator is the integral (or sum) of the absolute value of the contributions to the current. These expressions are evaluated around the vertices of the simulation grid. Clearly, c ranges from 0 (in a potential-field region) to 1 (in a maximally strong current-carrying region). In regions with $c \leq c_1$ the grid is allowed to coarsen, while in regions with $c \geq c_2 > c_1$ the grid is required to refine, constrained by the global minimum and maximum refinement levels permitted in the simulation. For the simulations in this paper, we used $c_1 = 0.02$ and $c_2 = 0.08$. In order to concentrate the fine grids in coronal current sheets where the field strength is relatively low, we also required that the average tangential field strength

$$\langle |B_t| \rangle \equiv \frac{\oint_C |\mathbf{B} \cdot d\mathbf{l}|}{\oint_C dl} = \frac{\sum_{n=1}^i |B_{t,n} l_n|}{\sum_{n=1}^i l_n}$$

satisfy $B_1 \leq \langle |B_t| \rangle \leq B_2$, where we chose $B_1 = 0.01$ G and $B_2 = 0.30$ G. The grid was tested for adaptation every 25 s by applying these criteria to each of the three components of the current. In addition, the two blocks immediately above the inner boundary were maintained at the highest refinement level throughout the simulation, to ensure that the boundary flows and associated currents were consistently well resolved. Figure 2 shows a

close-up of the grid at the peak of the impulsive flare phase (see §3), illustrating the ability of our selected adaptivity criteria to resolve the breakout, flare, and flux-rope current sheets.

We have developed diagnostic tools for quantitatively measuring reconnection via the identification and characterization of magnetic null points in the system. As demonstrated in §3, this capability proved crucial for a variety of tasks, from determining the velocity profile and spatial aspect ratio of the CME to ascertaining the time-dependent number of X-type cusps and O-type islands in the flare and breakout sheets. After averaging *ARMS*' primitive face values of B_r and B_θ to their adjoining cell edges, we first identify those grid blocks and individual cells across which both components switch sign (Greene 1992). Next, we fit a bilinear form to B_r and B_θ across each such identified cell and determine whether there is an interior solution to $B_r = B_\theta = 0$ (Haynes & Parnell 2007). If a solution exists, we have found a candidate null point. We then evaluate the Poincaré topological index (Arnol'd 1992) around the boundary N of the cell,

$$\text{ind } N = \frac{1}{2\pi} \oint_N \frac{B_\theta dB_r}{B_r^2 + B_\theta^2} = \frac{1}{2\pi} \oint_N d\arctan\left(\frac{B_\theta}{B_r}\right).$$

This index is 0, -1 , and $+1$ for vector fields (B_r, B_θ) having no nulls, a single X-type null, and a single O-type null, respectively, within N . To measure the isolation of the identified nulls, the index also is evaluated around 3×3 and 5×5 patches of cells centered on the original null-hosting cell. We assign *orders* $O = \pm 1, \pm 2$, and ± 3 to nulls having the same index ± 1 around only the cell itself, the cell plus its 3×3 patch, and the cell plus both its 3×3 and 5×5 patches, respectively. Spot checks of nulls with orders other than ± 3 have revealed consistently that this is due to algebraic cancellation of neighboring nulls of opposite types falling within the integration contour N , as expected from the topological theory (Arnol'd 1992). Finally, we ascertain the structural character of each null by evaluating the determinant of the matrix \mathbf{M} characterizing the local magnetic field, $\mathbf{B} = \mathbf{M} \cdot \delta \mathbf{r}$ (Parnell et al. 1996):

$$\mathbf{M} = \begin{pmatrix} +p & q-j \\ q+j & -p \end{pmatrix}$$

The parameters p and q of the symmetric part of \mathbf{M} are associated with the current-free (potential) part of the field, while the asymmetric contribution j is proportional to the electric current density. We introduce the dimensionless *degree* D of each null point,

$$D \equiv \frac{j^2 - p^2 - q^2}{j^2 + p^2 + q^2},$$

which can be calculated immediately from the slopes of the bilinear fits at the null. This normalized determinant of \mathbf{M} ranges from -1 ($j = 0$) for potential fields with X-type nulls through 0 ($j^2 = p^2 + q^2$) for sheet-type transitional nulls to $+1$ ($j^2 \gg p^2 + q^2$) for strong current-carrying O-type nulls with circular flux surfaces (see Figure 2 in Parnell et al. 1996). The opening angle χ of the X-type null hyperbola is

$$\chi = \arctan \sqrt{-\frac{2D}{D+1}},$$

which decreases from 90° to 0° over its range $-1 \leq D \leq 0$; at $D = -1/2$, $\chi \approx 55^\circ$. The eccentricity ε of the O-type null ellipse satisfies

$$\varepsilon^2 = \frac{\sqrt{1+D} + \sqrt{1-D}}{\sqrt{1+D} - \sqrt{1-D}},$$

which declines from ∞ to 1 over its range $0 \leq D \leq +1$; at $D = +1/2$, $\varepsilon \approx 2$.